Loess and floods: late Pleistocene fine-grained valley-fill deposits in the Flinders Ranges, South Australia

(excerpt from Hans Heysen 1929: “Foothill of the Flinders”, Morgan Thomas Bequest Fund 1939)

David Haberlah

Geology and Geophysics
School of Earth and Environmental Sciences
The University of Adelaide

This thesis is submitted in fulfilment of the
requirements for the degree of Doctor of Philosophy
in the Faculty of Science, University of Adelaide

August 2009

3. Results and Discussion

'Pray observe I do not pretend to say your theories are not right, but a substratum of facts ought surely to be first given.[...] Again I am sure the publication of your Loess views in their present state would injure your reputation: it is a most curious and difficult subject.' – Charles Darwin (Letter 780 to Adolph von Morlot 10th Oct. 1844)

The outcomes of the litho- and chronostratigraphic mapping and geophysical and geochemical laboratory analyses are presented and discussed in three separate papers. The results of the sediment-sizing study from the layered to laminated stratigraphic section at the confluence of the Aroona and Brachina Creeks are presented in the previous section 2.3, because of the overall methodological focus of this paper. The chronostratigraphy of BRA-AR and 12 other sections from all three catchments are discussed in detail in the book chapter of section 3.1. Finally, a high-resolution multi-proxy study performed on the layered to laminated section BRA-SD is presented as a manuscript in section 3.2. Here, the results of detailed lithostratigraphic mapping, parametric sediment-size analysis, quantitative mineral spectroscopy, induced magnetic susceptibility and carbon isotopic geochemistry are discussed in terms of potential palaeo-environmental scenarios.

Haberlah, D., Glasby, P., Williams, M.A.J., Hill, S.M., Williams, F., Rhodes, E.J., Gostin, V., O'Flaherty, A. and Jacobsen, G.E. (2009) 'Of droughts and flooding rains': an alluvial loess record from central South Australia spanning the last glacial cycle in *Australian Landscapes*, ed. Bishop, P. & Pillans, B., Geological Society of London Special Publications, v. 346, pp. 185-223.

Loess and floods: high-resolution multi-proxy data of Last Glacial Maximum (LGM) slackwater deposition in the Flinders Ranges, semi-arid South Australia

(similar version in submission with Quaternary Science Reviews)

David Haberlah [1, 2], *Martin A.J. Williams* [3], *Galen Halverson* [1], *Steven M. Hill* [1, 2], *Tomas Hrstka* [4, 5], *Alan R. Butcher* [6], *Grant H. McTainsh* [7], *Peter Glasby* [3]

[1] Geology & Geophysics, School of Earth and Environmental Sciences, University of Adelaide, Adelaide, SA 5005, Australia (david.haberlah@adelaide.edu.au, +61 (0)8 8303-8022)

[2] Cooperative Research Centre for Landscape Environments and Mineral Exploration

[3] Geographical & Environmental Studies, School of Social Sciences, University of Adelaide, Adelaide, SA 5005, Australia

[4] SGS Minerals Services, QLD 4064, Australia

[5] Institute of Geology, Czech Academy of Science, Rozvojova 269, 165 02 Prague 6-Lysolaje, Czech Republic

[6] FEI Australia, Brisbane, QLD 4064, Australia

[7] Atmospheric Environment Research Centre, Griffith University, Brisbane, QLD 4111, Australia

Abstract

Terrace remnants of late Pleistocene fine-grained valley-fill formations (Silts) deeply entrenched by ephemeral traction load streams in arid areas remain a puzzle. They have been attributed to a variety of origins ranging from lacustrine to alluvial floodplains. We here report a centimetre-scale multi-proxy study of a 7 m section of similar Silts in the semi-arid Flinders Ranges of South Australia, which span the lead-up to and peak of the Last Glacial Maximum. The results of detailed lithostratigraphic mapping, high-resolution parametric particle-size analysis, quantitative spectral mineralogy, magnetic susceptibility, carbon stable isotope geochemistry, and a chronostratigraphy based on 27 AMS radiocarbon and 6 luminescence ages are discussed in terms of sediment provenance, depositional environment, weathering and local hydrology with the aim of reconstructing the regional hydroclimatic history. The data are consistent with inferences of a fluctuating aeolian-fluvial interplay dominating the extended LGM environment with a greater impact on the landscape than all geomorphic processes since then. Accordingly, proximal dust accessions (loess mantles) were eroded and entrained by numerous small and at least a dozen large-scale flood events and trapped in an intra-montane floodplain extending into Brachina Gorge. Upstream of this narrow constriction, recurrent backflooding is discussed resulting in a thick sequence of slackwater couplets. Aggradation and degradation of the valley-fills appear to be largely controlled by sediment supply from the valley slopes, possibly replenished by aeolian dust accessions from upwind deflated terminal playa lakes and dunefields. In conclusion, this study demonstrates how dust storms and flooding rains can account for 'pluvial' features previously explained by the opposing effects of reduced precipitation and evaporation in the colder more arid glacial landscape of southern Australia.

Introduction

The contrast between gently sloping, deeply entrenched fine-grained valley-fills and rugged chains of weathering-resistant ridges that inspired the painter Sir Hans Heysen (1877-1968) in the Flinders Ranges of South Australia have prompted more recent scientific interest. Cock et al. (1999) first described a laminated sequence of silts within Brachina Gorge in the central Flinders Ranges as spanning the Last Glacial Maximum (LGM) (Fig. 1; Plate 1). The LGM (24-18 ka: EPILOG LGM chronozone Level 2; Mix et al., 2001) is elsewhere in south-eastern Australia marked by widespread erosion, deflation of lake beds and salt pans (playas), and actively migrating dunefields (e.g. Fitzsimmons et al., 2007). Yet, here is a continuous more than 7 m thick aggradational sequence of well-defined centimetre-scale laminations, extending horizontally for hundreds of metres and, judging by its fine-grained texture and redoximorphic colours, suggestive of lacustrine deposition (Cock et al., 1999). A year later, a theodolite survey established that the surface of the Brachina Silts is inclined westwards with a mean gradient of 1:87, parallel to the present-day thalweg and older rock-cut benches (Williams et al., 2001). The spatially restricted, layered to laminated facies is embedded in a fluvial massive tabular facies that extends into Brachina Gorge where it is preserved as terraces up to 18 m high. Williams et al. (2001) discuss “the enigma of a late Pleistocene wetland” and concluded that an aggraded surface with this slope was ‘incompatible with sedimentation in a shallow lake’ (op. cit., p.133). They concluded that ‘the clays and fine sands accumulated in a fluvial wetland, essentially unchannelled in the fine-textured reaches but entered at its margins by channels carrying coarser sediment from tributary streams and fans’ (op. cit., p.133). Three hypotheses were proposed addressing provenance, depositional nature and the demise of the valley-fills. **1)** The fine-grained material, in stark contrast to today’s gravel- and sand-dominated stream bed, entered the catchment as proximal dust. **2)** The aeolian accessions were eroded by gentle winter rains, trapped by swamp vegetation and aggraded in the form of a mainly channel-free “fluvial wetland”. **3)** Terminal incision, heralded by an influx of coarse alluvium, was triggered by storm-driven floods likened to the monsoonal incursions that at present inundate floodplains in the region at decadal to centennial frequency (McCarthy et al., 2006). The first hypothesis was supported by: **a)** aggradation rates far in excess of long-term catchment erosion rates as inferred from *in situ* cosmogenic ^{10}Be-measurements (Williams et al., 2001); and, **b)** by a comparative geochemical study of loess patches from the slopes, valley-fill remnants and the bedrock geology (Williams and Nitschke, 2005). The second hypothesis complies with the “minevaporal theory” of Galloway (1965), often invoked in Australia to explain “pluvial” anomalies such as high lake beach ridges dated to the glacial interval otherwise characterised by peak aridity. It was since confirmed as a potential catchment scenario by modelling the impact of lower glacial temperatures and the retreat of the dominant riparian tree river red gum (*Eucalyptus camaldulensis*) on the local hydrology by: **a)** lowering the cloud base, thereby increasing orographically enhanced “drizzling” winter rainfall; and, **b)** by significantly reducing evapo-transpiration and raising local water tables (Williams et al., 2006). However, this low-energy depositional scenario contrasts with most recent interpretations of similar LGM deposits of loess-derived alluvium in Namibia (Eitel et al., 2001) and the Sinai Peninsula (Rögner et al., 2004), suggested to reflect more frequent and intense run-off events (Lancaster, 2002; Heine and Heine, 2002; Srivastava et al., 2005). Furthermore, the very stratigraphic type section that prompted the initial scientific interest (Cock et al., 1999) remained at odds with a wetland scenario, in which swamp vegetation and other forms of bioturbation would have destroyed the laminations. This study addresses the layered to laminated aggradational sequence by an integrated lithostratigraphic, chronostratigraphic, geochemical and geophysical approach, aiming to establish the provenance of the material, its depositional, weathering and hydrological history, changes in the vegetation cover of the catchment and the regional climate throughout the LGM, which according to several recent reviews was far more complex than previously assumed (Gasse et al., 2008; Williams et al., 2009).

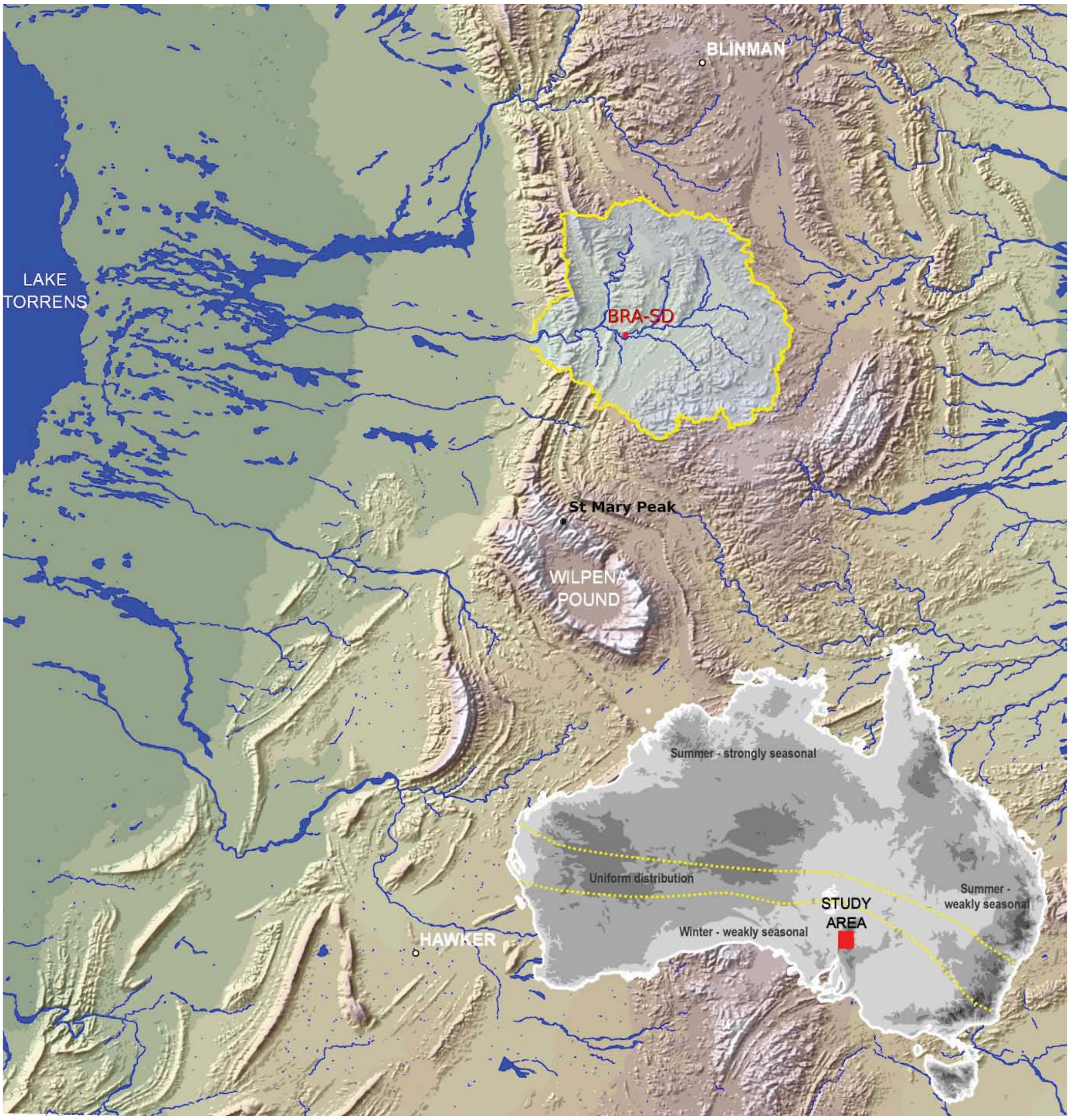

Fig. 1) Study area: *location of the layered to laminated stratigraphic section BRA-SD within the Brachina catchment as outlined in yellow. Major creeks and water bodies draining the Flinders Ranges to the west towards terminal playa Lake Torrens, and to the east towards terminal playa Lake Frome are projected in blue. The inset figure places the study area on the Australian continent (SRTM DEM) and in context of present-day seasonality (adapted from Gentilli, 1986).*

Stratigraphic type section BRA-SD

The main body of the Brachina Silts spreads for ~2 500 m from east to west across the middle reaches of the Brachina valley, increasing in thickness and converging upon the steep weathering-resistant range front of the ABC Quartzite (Cock et al., 1999) (Fig. 1 & 2). The layered to laminated facies is spatially restricted to the Brachina-Etina confluence upstream of the narrow Brachina Gorge that cuts through the quartzite ridge. The stratigraphic type section BRA-SD describes the distal reaches of a ~235 m long semi-circular vertical cliff face more than 7 m thick consisting of alternating light and dark layers and laminations banked against the steep vegetated valley slope (Photo 1). The sediments are undercut and eroded by the present course of Brachina Creek except where unconformably resting upon jagged bedrock of Neoproterozoic shales that underlie the Silts (Photo 2A, Fig. 2) (Preiss, 1987).

Lithostratigraphy

The stratigraphic section includes five lithostratigraphic units (Photo 1; appendix 5.3A). From the base up these consist of:

1) **Basal unit (I)** 700-506 cm (below top): Overall red-brown sequence of decimetre-thick alternating lighter and darker bands with transitional boundaries terminating in a well-defined dark brown/grey (5YR 6/1 $_{\text{dry}}$ / 7.5YR 5/1 $_{\text{moist}}$) band of blocky to prismatic structure and slickensides at 506 cm, previously interpreted as a palaeosol (Cock et al., 1999; Williams et al., 2001). The thickness of the transitional bands decreases towards the top of the unit. In contrast to the exclusively fine-grained units above, multiple sheets of rolled detrital calcareous nodules (transported pedogenic carbonate sourced from reworked Bca-horizons) (Photo 2B), large (>5 cm) pieces of charcoal (Photo 2C), and a single line of well-rounded cobbles and tufa clasts (Photo 2D) are incorporated. In rare instances, current cross-bedding is faintly preserved. At the base, vertical *in situ* calcareous rhizomorphs are exposed (Photo 2E). A few large pseudogleyic root casts extend from the overlying sediments into the basal unit (Photo 2F).
2) **Transitional unit (II)** 506-470 cm: Onset of laminated aggradation bracketed by a light yellowish brown “yellow band” at 500 cm and a light reddish brown “red band” at 470 cm (Photo 3A). The sequence differs from the laminated unit (III) above in its overall more oxidised appearance reflecting that of the basal unit (I) (Photo 1), and in that the yellow and red bands thicken towards the upstream valley slope.
3) **Laminated unit (III)** 470-90 cm: Alternating light and dark laminations including ten ~10 cm thick “yellow bands” that stretch across the width of the section and extend towards the present-day Brachina-Etina confluence, increasing in thicknesses to >20 cm. Where the laminations are disturbed, the sharp boundaries grade into thicker pale and dark bands.
4) **Pedogenic unit (IV)** 90-0: The laminations become increasingly disturbed by pedogenesis and bioturbation. Precipitation of soft pedogenic carbonate nodules (Bca-horizon), root casts, animal burrows and desiccation cracks obliterate veneers of organic detritus above ~60 cm. At this

level, the sudden appearance of mostly locally-derived gravel supersedes the exclusively fine-grained depositional regime.

5) **Surface drape (V)** up to 10 cm thick: Yellowish red platy fine-grained mantle that covers the top of the section and most of the alluvial plain. In places, it drapes steep erosional gully banks (Photo 3B), indicating post-incisional deposition yet to be dated.

The central sequence of laminations (II&III) includes three lithofacies (Photo 3A):

a) **Yellow bands** (red band): Light yellowish brown (2.5Y 6/4 $_{\text{dry}}$/ 5/4 $_{\text{moist}}$) and light reddish brown (5YR 6/3 $_{\text{dry}}$/ 7.5YR 6/3 $_{\text{moist}}$) friable granular silt and very-fine sand mantling underlying sediments as discrete sheets. A dozen are close to 10 cm thick and continuous (Photo 1). Despite their overall excellent preservation, sedimentary structures, such as cross-stratification, were not identified. In some parts, small pieces of charcoal are incorporated. Together with 22 discrete, only centimetre-thin, and 20 more disturbed often mottled yellow bands, this lithofacies makes up two thirds of the laminated sequence (appendix 5.3A). Upper boundaries are typically blurred, with vertical millimetre-thick channels extending from the overlying lithofacies, introducing dark organic-rich material.

b) **Organic veneers**: Similar fine-grained sediments hosting stacked undulating veneers of black plant detritus, dominated by elongated phytoliths with bulliform and quadrilateral cells characteristic of grasses (Williams et al., 2001). The 33 best preserved veneers mostly overlie yellow bands and range in thickness between <1-4 cm. Together with 25 dark bands of disturbed veneers of up to 5 cm thickness, organic veneers contribute to a quarter of the laminated sequence (II&III) (appendix 5.3A). The veneers are best preserved where associated with tufa.

c) **Tufa**: White discontinuous streaks of carbonate precipitation, loosely cemented and typically associated with organic detritus. The tufa closely resembles carbonate precipitation observed west of the Ranges in shallow evaporating pools in the aftermath of the January 2007 flood (Photo 2G). Tufa bands of up to 5 cm thickness provide ~8 % of the laminated sequence (II&III) (appendix 5.3A), but only two bands are continuous enough to be included in the type section drawing (Photo 1).

The three lithofacies largely follow a cyclic stacking pattern: yellow bands are topped by organic veneers that alternate and interfinger with streaks and thin sheets of tufa (Photo 3A). Transitions between the different lithofacies are usually sharp and, except for the 12 continuous yellow bands, undulating. No erosional contacts were observed, but upper boundaries of the yellow bands are often blurred by bioturbation.

Imbrication Patterns

Discrete gravel facies were restricted to one narrow line of well-rounded cobbles (Photo 1; 2D) within the stratigraphic section. Elsewhere across the deeply dissected alluvial plain however, numerous clast-supported gravel-fills are exposed as chutes and sheets. The main imbrication direction was mapped for all significant gravel exposures with the aim to reconstruct dominant flow patterns throughout the aggradation of the Silts (appendix 5.3B). The gravel occurrences are grouped into three colour-coded categories as a function of their depth below surface (i.e. their relative age): **1)** onset of aggradation (green); **2)** main aggradational interval (yellow); and, **3)** termination (red) (Fig. 2). The lowermost gravel exposures largely consist of thick narrow channel-fills, approximating present-day flow directions of the entrenched Brachina and Etina Creeks and in places fan out across the bedrock surfaces. With advanced Silt aggradation, there is a marked deviation from the present-day channel network. Accordingly, the Brachina tributary discharge flowed across the alluvial plain into Etina upstream of the modern confluence (Fig. 2). In contrast, the main flow axis of the Etina Creek remained much the same. The locality of the laminated stratigraphic section was partially shielded by raised bedrock outcrops and occupied a peripheral position. According to a sequence of shallow superposed gravel beds in the proximity of the modern confluence (Fig. 2) that display reversed directions of inclination (“herringbone pattern”) (Photo 3C), the site was repeatedly inundated by water flowing out of and into the main axis of flow. Towards the termination of the fine-grained depositional regime, the Etina/Brachina overflowed the complex bedrock topography of today’s confluence. Further upstream, the termination is characterised by gravel sheets extending across the alluvial plain, mantled only by the surface drape. The long α-axes of the inclined gravel clasts are orientated more often parallel than perpendicular to the palaeoflow direction, possibly indicating a hyperconcentrated high-energy flood depositional environment (Rust, 1972; Hartley et al., 2005), however further quantitative analysis of the gravel lithofacies is required.

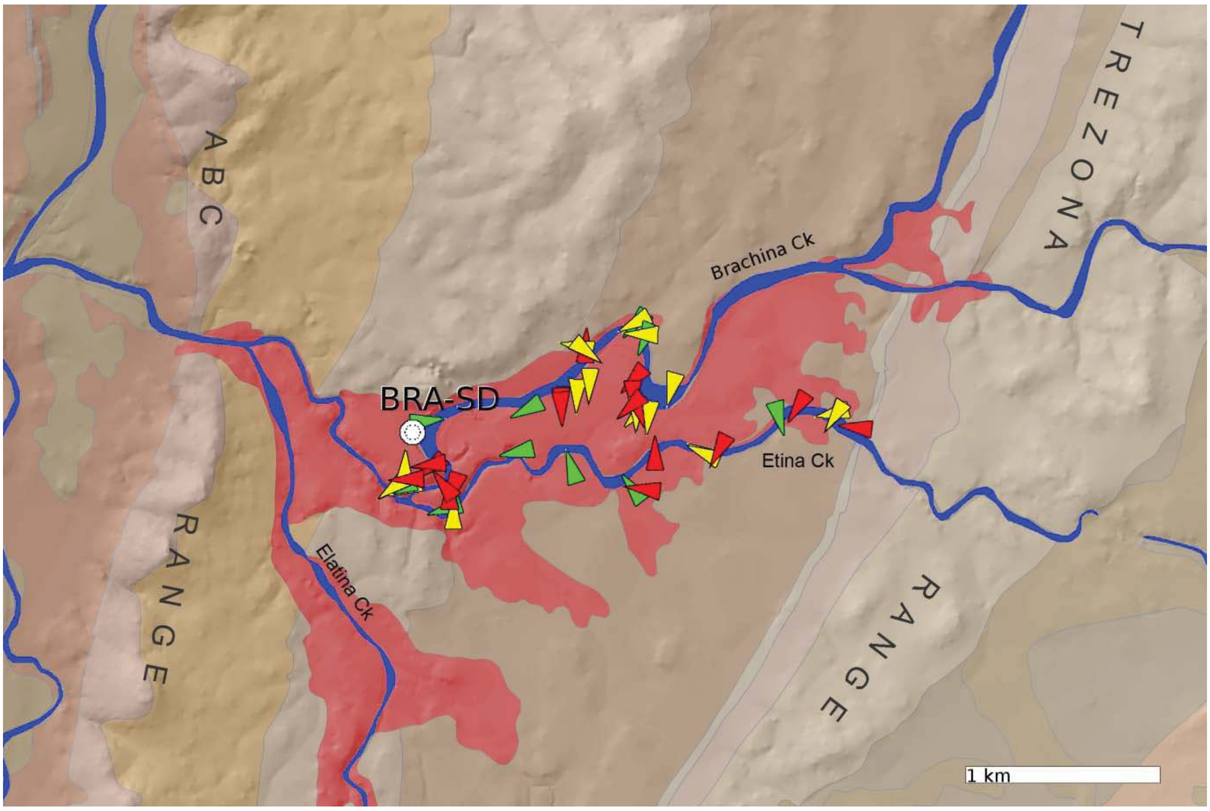

Fig. 2) Drainage pattern: *evolution of flow directions throughout the aggradation of the Brachina Silts as inferred from main imbrication directions measured from inset gravel exposures along the Brachina and Etina Creek beds. The fine-grained valley-fills are colour-coded in **shaded red** and the stratigraphic section BRA-SD is indicated in white. The arrows point towards palaeo-flow directions of mapped gravel chutes and sheets. Their relative depth below the highest floodplain surface is presented by three colours and corresponds to the main lithostratigraphic units of BRA-SD (see appendix 5.3B): **green** refers to the onset of fine-grained aggradation with gravel exposures resting on or closely above the bedrock (= basal unit I); **yellow** refers to gravel exposures cut into or aggrading throughout the main aggradational phase (= laminated units II&III); and, **red** refers to gravel sheets that spread out across the fine-grained floodplain, usually mantled only by the surface drape (= pedogenic unit IV).*

Sediment-size analysis

Texturing of the fine-grained valley-fills presents a challenge in that the material invariably consists of silt loam, sometimes becoming “heavier” (more clayey) with continued working by hand. This soil property, termed “subplasticity”, is widely reported from loess-derived sediments throughout south-eastern Australia (e.g. Butler, 1955; McIntyre, 1976). In order to obtain a detailed and genetically more meaningful picture of the sediment composition, a two-step approach was performed involving: **1)** high-resolution 3-D sediment-sizing by the electrical sensing zone method employing the Multisizer™ 3 COULTER COUNTER® (Beckman Coulter, 2002); and, **2)** conventional and parametric analyses of the statistical particle-size distributions. Eleven samples from key yellow bands and other significant strata were first described by standard statistical derivatives. Then, discrete principle particle populations that make up the size distribution were quantified for both partially aggregated (minimally-dispersed) and particulate (fully-dispersed) sample conditions. The granulometric results are interpreted in terms of sediment provenance and depositional mode.

Protocol

The consolidated sample material was immersed in ISOTON II (1 g/100 ml), left to slake, and stirred in a baffled beaker, maintaining a uniform suspension throughout sub-sampling by pipette. This treatment breaks up loosely-bound aggregates, but further dispersion is soon resisted. The sample state is described as its minimally-dispersed (MD) condition (Leys et al., 2005) and assumed to survive non-laminar water flow (Schieber et al., 2007; Haberlah and McTainsh, subm.). Consequently, the sediment suspension was dispersed by means of ultrasonic bath (Branson 2 200 sonifier, 472 Hz/ 60 W for 30 min) and hydrochloric acid (1 % HCl), removing carbonate cementation, tufa and shells. Sample suspensions were diluted to concentrations of 5-10 % and passed through an array of calibrated orifice tubes (560, 280, 140 & 50 µm) covering the nominal particle-sizing range between 1-336 µm with generous overlap. A minimum sizing threshold of 3-4 µm was employed to eliminate the effect of electronic interference caused by iron-rich particles that resulted in some abnormal electrical pulses towards the lower size limit. Hence, clay particle contributions (<3.9 µm) are truncated. The size fraction >200 µm was wet-sieved for ~300 g of sample material. Results are expressed in weight percentage (appendix 5.3C), described, and photographed under binocular microscope. The silt- to sand-sized particle-size distributions (PSDs) are based on >1 000 000 analogue pulses that were converted and merged into 256 discrete size classes of sub-micron resolution. Standard statistical derivatives such as percentiles, mean, mode, skewness and kurtosis (Inman, 1952; Folk and Ward, 1957) were described by the Beckman Coulter Multisizer™ software (Beckman Coulter, 2002) (Fig. 3; appendix 5.3C). Consequently, the PSDs were converted into log10-listings and imported into the “Mixdist” library (Macdonald and Du, 2004) as part of the “R” environment for statistical computing (R Team, 2008). The Particle Size Distributions (PSDs) were resolved into 2-4 discrete stretched-exponential (Weibull) distributions interpreted as the principal particle populations that make up the sediment (Folk, 1971; Sun et al., 2002; Leys et al., 2005; Haberlah and McTainsh, subm.). The iterative computation, employing a Newton-type algorithm and the expectation-maximisation algorithm, was initiated by specifying 5 evenly-spaced unconstrained end-members, and progressed by eliminating insignificant (<1 %) and redundant populations (Haberlah and McTainsh, subm.) (appendix 5.3C).

Results

All **fully-dispersed** (FD) samples are predominantly composed of silt (3.9-62.5 µm) (Fig. 3). Most yellow bands further display a significant very-fine sand component (62.5-125 µm) but, in contrast to samples from the basal unit (I) and the uppermost section (IV&V), little to no coarse material. The coarser 275-285 yellow band is an exception by comprising ~8 % fine sand. The PSDs of the yellow bands are narrow and peaked, with coarse silt to very-fine sand (20-125 µm) invariably making up >75 % of the sediment volume. All sample modes fall within a narrow range of 50-63 µm, except for the 470-479 red band. Here, a 71 µm mode indicates the presence of coarser material, but the median particle size of 60 µm still lies within the silt size range. Negative skewness, here expressed by modes larger than corresponding median values (Fig. 3), is evident in all but the near-symmetrical distribution of the lowermost sample (650-660) and reflects the presence of additional fine sediment. In the top sample (000-010), this fine component is particularly pronounced, resulting in a bimodal distribution. Aggregation is assessed by juxtaposing corresponding FD and **minimally-dispersed** (MD) particle-size distributions and their statistical derivatives (Fig. 3). For most samples, differences between the two are negligible. An increase of >5 % in the silt fractions is only recorded for the coarser 275-285 yellow band and the two uppermost samples (IV&V). This increase corresponds with a decrease in the >62.5 µm fractions, indicating the presence of sand-sized mud aggregates. A comparison between ratios of mode and median values for both sample conditions show that PSDs are more symmetrical in MD condition. A genetically meaningful quantitative description of the sediment composition and nature of aggregation is attempted by parametrically resolving the distributions into their **principle particle populations**. Accordingly, the primary particle population consists of coarse silt with modes ranging from 40-64 µm contributing >75 % to all yellow bands (Fig. 3). The 348-355 yellow band, in which this population attains only 72 %, wedges out in the section face and exhibits a larger fine silt particle population. This poorly-sorted secondary population is present in all samples with an average mean and mode of 16 µm. In samples from the palaeosol, transitional unit (II), and termination of the sequence (VI&V), the fine silt particle population is more abundant than in the yellow bands of the laminated unit (III). The two lowermost and uppermost samples and the coarser 275-285 yellow band further comprise a fine sand tertiary particle population (Fig. 3). With the exception of the basal unit (I), this coarse particle population is resolved in corresponding FD sample conditions, indicating that it is made up of mud aggregates. With the exception of the coarser 275-285 yellow band, >99 % of the material of the yellow bands is made up of particles <200 µm. This is in contrast to the basal (I) and uppermost sediments (IV&V) that respectively consist of 1⁄10 and ⅓ of sand -sized well-rounded quartz grains (Photo 3D), gastropod shells (Photo 3E), charcoal (Photo 2C) and tufa fragments, and lithic clasts (appendix

5.3C). Between 506-380 cm, a succession of thin, less-continuous laminations, in places incorporating streaks of tufa and topped by veneers of organic detritus (Photo 3A), was sized in MD condition (Haberlah et al., 2007). Results indicate a succession of upward-fining couplets, as expressed by a decrease in the coarse silt primary particle population accompanied by an increase in the fine silt secondary particle population. In the representative example (Fig. 3), the volume contribution of the 43 µm primary particle population decreases with subsequent deposition of material associated with *in situ* tufa formation and plant detritus, to the point where the 11 µm secondary particle population makes up the bulk of the material.

Data interpretation

The texture of the sediments remains remarkably similar throughout the aggradational sequence, principally consisting of coarse silt and very-fine sand. The narrow size range and the steep drop-off in coarse material are attributed to the aeolian provenance of the material. As proximal dust, the material was carried in suspension across the steep range front into the catchment, with the upper size limit controlled by maximum wind velocities. The high-resolution particle-size distributions, and their decomposition into principle particle populations, reveal subtle but important variations in sorting and the presence of transport-stable mud aggregates. The sedimentary fraction that straddles the Wentworth boundary between silt and sand (62.5 µm) dominates all samples but is particularly expressed in the narrow and peaked (leptokurtic) particle-size distributions of the yellow bands. Their well-sorted composition is best explained by additional sorting of the former loess mantles during fluvial entrainment, transport and deposition. The primary and secondary particle populations were collectively transported in suspension by turbulent flow. With the reduction in flow capacities as a result of backflooding from the narrow gorge entrance, the coarse silt particle population settled out of the water column more rapidly than the fine silt population. This interpretation is consistent with an increase in the fine silt population in overlying material associated with plant flotsam, and in the finer 348-355 yellow band that pinches out in the section face and hence reflects the distal reach of the associated inundation event. In contrast, the lowermost (I) and uppermost (IV&V) samples are less sorted and incorporate lithic sands. They are more likely to have been deposited as fluvial bedload or colluvium from adjacent loess-mantled slopes. A comparison between corresponding MD and FD particle-size distributions suggests that these samples, and the 244-250 tufa-bearing yellow band, also comprise transport-stable mud aggregates primarily made up of fine silt. All minimally-dispersed sample expressions exhibit the better defined modes as expressed by a shift from platykurtic to leptokurtic, or in the case of sample (000-010), from bimodal to unimodal particle-size distributions. This observation is interpreted to reflect pre-depositional aggregation, with mud aggregates possibly formed during fluvial transport

(Schieber et al., 2007), and corroborates a study conducted downstream concluding that loess-derived alluvium is best characterised by minimally-dispersed sediments (Haberlah and McTainsh, subm.).

(see opposite page)

Fig. 3) Multisizer™ 3 COULTER COUNTER® samples: *particle-size distributions (PSDs), key statistical derivatives and parametrically-resolved principle particle populations. Mode (MD) and median (d50) particle sizes are listed for both samples states, with black numbers referring to minimally-dispersed and white numbers to fully-dispersed samples. The PSDs are presented as particle sizes (in µm) on a logarithmic scale versus the normalised volume, with size boundaries of clay/silt (3.9 µm), silt/very-fine sand (62.5 µm) and very-fine sand/fine sand (125 µm) indicated by dotted lines. The sedimentary fractions are quantified in terms of fine (3.9-20 µm) and coarse silt (20-62.5 µm), very-fine sand (62.5-125 µm) and fine sand (125-250 µm), and depicted as pie charts with blue colours referring to minimally-dispersed, and red colours to fully-dispersed sample modes (see legend). Parametrically-resolved, partially-overlapping principle particle populations are plotted in blue for minimally-dispersed, and red for fully-dispersed sample states. The population modes are indicated as black, white and grey triangles (see legend). The dominant principle particle population is listed as a mode/mean value (in µm) in the PSDs, with corresponding relative percentage to the right. Minimally-dispersed PSDs of a succession of laminations forming a representative slackwater couplet are superimposed, with partially-constrained modes highlighting the depositional size trends in the coarse silt and fine silt particle populations settling out over the course of flood fluxes (see legend).*

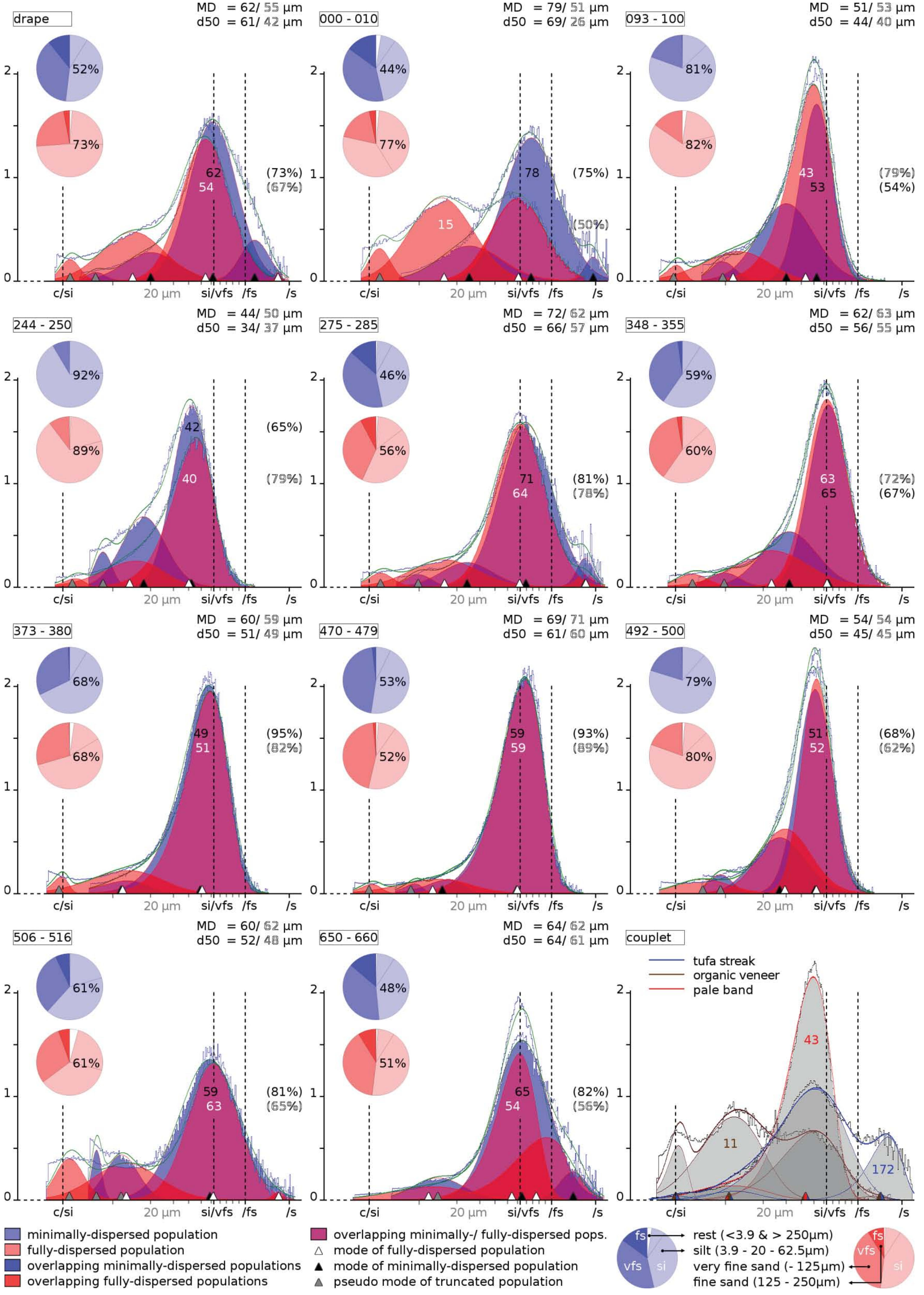
drape
MD = 62/ 55 µm
d50 = 61/ 42 µm
52%
73%
62
54
(73%)
(67%)
000 - 010
MD = 79/ 51 µm
d50 = 69/ 26 µm
44%
77%
15
78
(75%)
(50%)
093 - 100
MD = 51/ 53 µm
d50 = 44/ 40 µm
81%
82%
43
53
(79%)
(54%)
244 - 250
MD = 44/ 50 µm
d50 = 34/ 37 µm
92%
89%
42
40
(65%)
(79%)
275 - 285
MD = 72/ 62 µm
d50 = 66/ 57 µm
46%
56%
71
64
(81%)
(78%)
348 - 355
MD = 62/ 63 µm
d50 = 56/ 55 µm
59%
60%
63
65
(72%)
(67%)
373 - 380
MD = 60/ 59 µm
d50 = 51/ 49 µm
68%
68%
49
51
(95%)
(82%)
470 - 479
MD = 69/ 71 µm
d50 = 61/ 60 µm
53%
52%
59
59
(93%)
(89%)
492 - 500
MD = 54/ 54 µm
d50 = 45/ 45 µm
79%
80%
51
52
(68%)
(62%)
506 - 516
MD = 60/ 62 µm
d50 = 52/ 48 µm
61%
61%
59
63
(81%)
(65%)
650 - 660
MD = 64/ 62 µm
d50 = 64/ 61 µm
48%
51%
65
54
(82%)
(56%)
couplet
tufa streak
organic veneer
pale band
43
11
172
0
1
2
c/si
20 µm
si/vfs
/fs
/s
minimally-dispersed population
fully-dispersed population
overlapping minimally-dispersed populations
overlapping fully-dispersed populations
overlapping minimally-/ fully-dispersed pops.
△ mode of fully-dispersed population
▲ mode of minimally-dispersed population
▲ pseudo mode of truncated population
fs
vfs
si
rest (<3.9 & > 250µm)
silt (3.9 - 20 - 62.5µm)
very fine sand (- 125µm)
fine sand (125 - 250µm)

Mineralogy

Mineral spectroscopy was performed employing the QEMSCAN® technique which combines electron beam and backscattered electron (BSE) systems with scanning electron microscopy (SEM), X-ray mapping and liquid nitrogen-free energy dispersive spectrometers (EDS) (Gottlieb et al., 2000). Primary rock-forming minerals, secondary clay minerals, evaporites and iron oxides were quantitatively assessed in 13 undisturbed consolidated hand specimens, including all previously sized section face samples, the underlying bedrock and loose dune sand from the western piedmont plain. The polished sample surfaces were mapped by dedicated software (iDiscover™), providing additional spatial context, size and texture attributes. The mineral maps are interpreted in terms of their degree of particle sorting and the presence and nature of aggregation, bioturbation, and *in situ* formation of clay minerals, carbonates and iron oxides. Size dependencies of detrital primary mineral particle abundances are discussed in terms of sediment provenance, and as a potential proxy for palaeowind velocities (Kandler et al., 2009).

Protocol

The QEMSCAN® samples were ground and polished following an adapted vacuum epoxy treatment optimised to fixate larger, loosely-bound particles. Sample surfaces were scanned by QEMSCAN® 310-series instrument fitted with SIRIUS 10/SUTW detectors, employing electron beam stepping intervals of 15 µm over a total area of 100 mm^2. A site-specific regolith mineral Species Identification Profile (SIP) library was compiled. The ten most abundant minerals, as identified by bulk mineralogical analysis, are presented as colour-coded mineral maps. For all major constituents (>10 %), average mineral particle sizes were stereologically calculated from intercept lengths and boundary transitions (Sutherland, 2007).

Results

All specimens include an identical suite of dominant minerals except for a fluctuating carbonate content (Fig. 4). Quartz and feldspars account for more than half the sediment volume in all but sample (650-660) from the basal unit (I), the lowermost (492-500) and uppermost (093-100) yellow bands, in which clay minerals constitute the majority. The quartz fraction appears to control the overall composition more than any other constituent and has an inverse relationship with carbonates, but for the carbonate-free palaeosol and surface drape. The latter two stand out by a near-identical composition and corresponding average mineral particle sizes. The quartz fraction invariably constitutes the coarsest major component. Throughout laminated aggradation (II&III), mean quartz particle sizes gradually increase, peak and decrease, approximating the trend of their overall abundance in the samples (Fig. 4). The same size-trend is mirrored by K-feldspars, here however independent of their relative volume contribution. In contrast, the clay minerals do not exhibit vertical size-trends and fall within a narrow size range. Minerals of the bedrock sample remain below corresponding average mineral particle sizes in the overburden. Single mean particle-size values are problematic in samples with polymodal particle-size distributions, as evident in the dune sand. Its quartz component was digitally resolved into a mineral-size distribution that highlights the abundance of material in the silt to fine-sand size range (Fig. 5). The generation of mineral maps from polished surfaces of the samples provides additional size, shape and contextual information (Fig. 6). The high degree of sorting in the yellow (and red) bands throughout the interval of laminated aggradation (II&III) is in contrast to samples from the basal unit (I) and the uppermost sequence (IV&V) that incorporate sand-sized particles of quartz, mud aggregates, and carbonate and lithic clasts. All section samples comprise some quartz and K-feldspar particles larger in size than present in the homogenous fine-grained bedrock specimen, however abundant in the dune sample. The yellow bands differ in their degree of post-depositional bioturbation and pedogenesis. Irregular vertical channels of varying thickness lined by secondary clay minerals characterise the lower and uppermost yellow bands. The 470-479 red band and the 348-355 yellow band exhibit detrital root pseudomorphs cemented by iron oxide precipitation (Photo 3F). Carbonates occur either as homogenously dispersed clasts slightly larger in size than corresponding quartz particles (650-660, 470-479, 000-010), or as *in situ* precipitates (348-355, 093-100). The latter, wet-sieved and examined under binocular microscope, morphologically resembles cemented paludal tufa (Photo 3G) (Pedley, 2009).

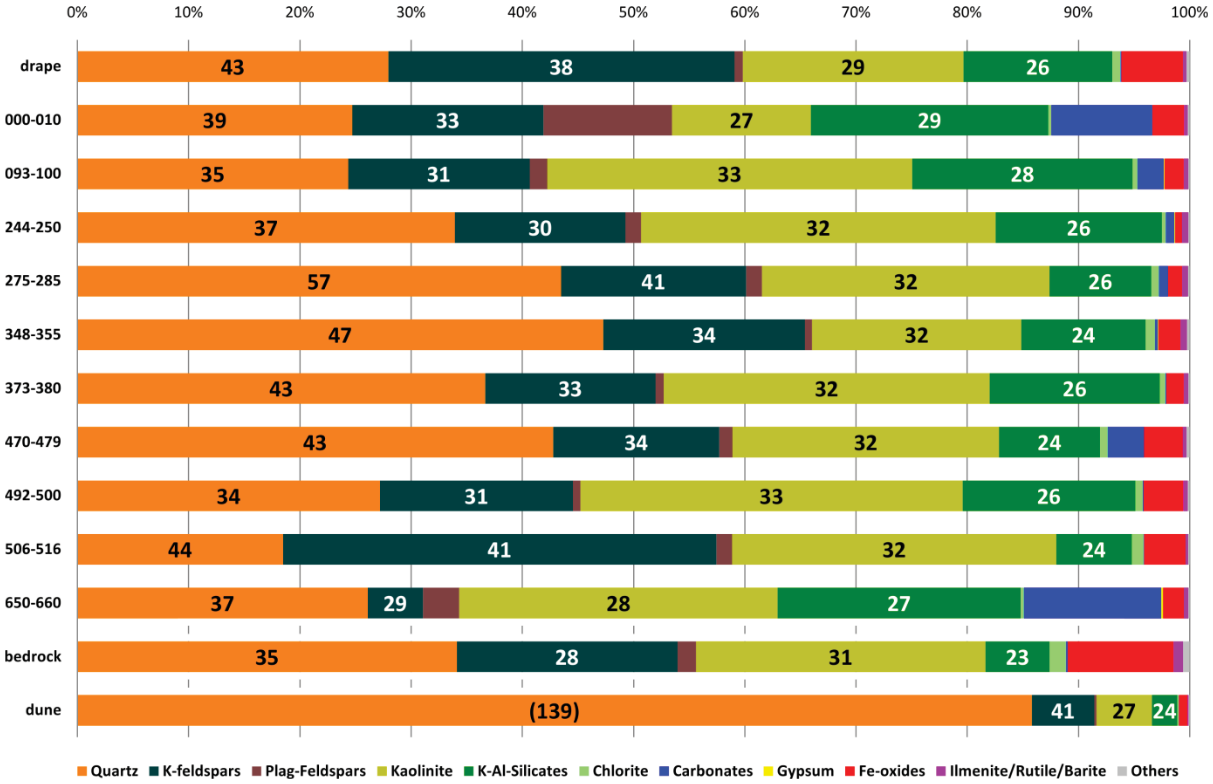

Fig. 4) QEMSCAN® samples: *bulk mineralogy and mineral particle sizes. Minerals are colour-coded (see legend) and presented as relative volume percentages in the sample. Stochastic mean mineral particle sizes are listed for all major constituents (>10 %) in the corresponding bar segments.*

(see opposite page)

Fig. 5) QEMSCAN® dune sample: *virtually-resolved particle-size distribution of the quartz component, highlighting its abundance in the coarse silt- (20-62.5 µm) and very-fine sand (62.5-125 µm) -sized fraction.*

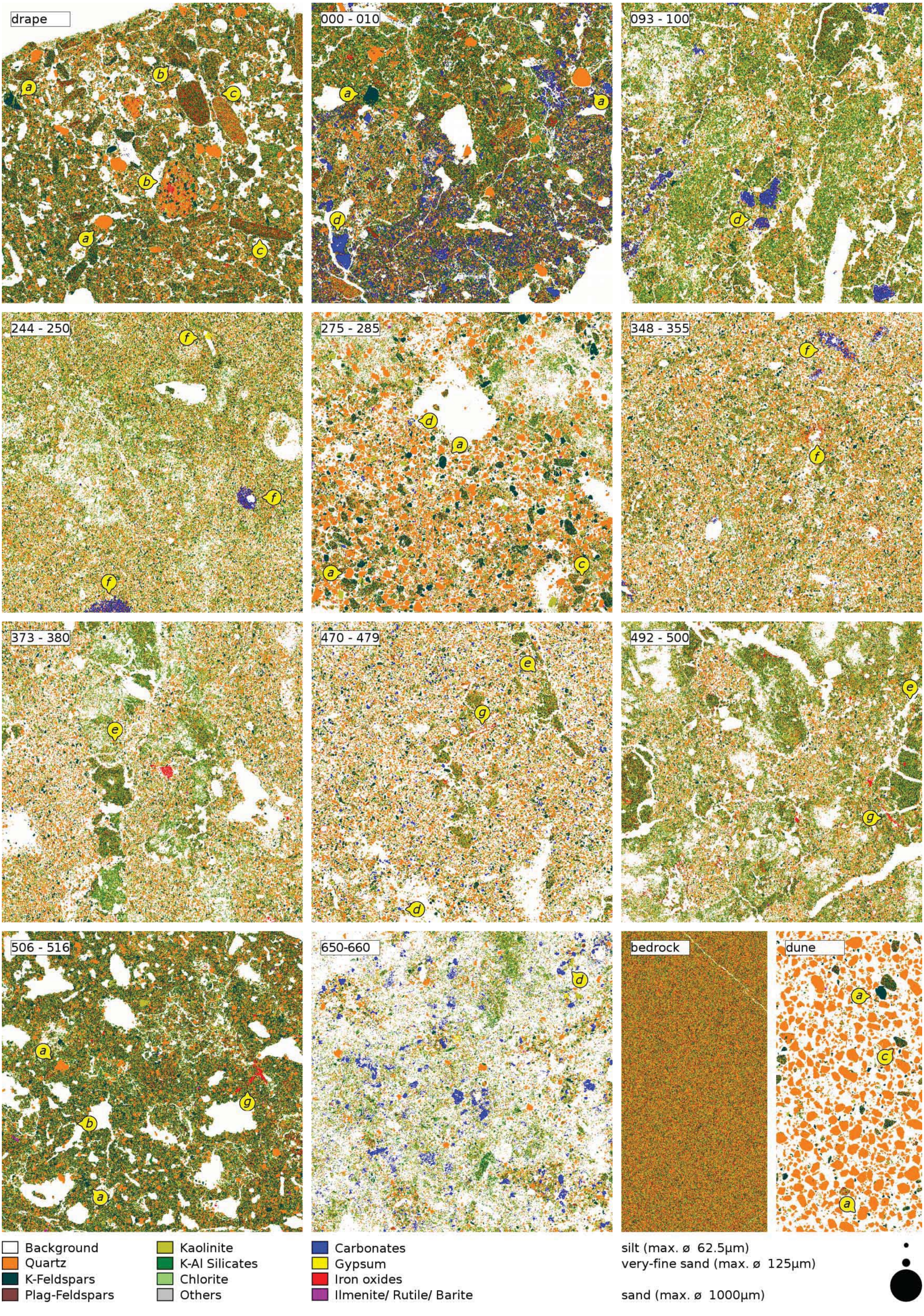
drape
000 - 010
093 - 100
244 - 250
275 - 285
348 - 355
373 - 380
470 - 479
492 - 500
506 - 516
650-660
bedrock
dune
a
b
c
d
e
f
g
Background
Quartz
K-Feldspars
Plag-Feldspars
Kaolinite
K-Al Silicates
Chlorite
Others
Carbonates
Gypsum
Iron oxides
Ilmenite/ Rutile/ Barite
silt (max. ø 62.5µm)
very-fine sand (max. ø 125µm)
sand (max. ø 1000µm)

Data interpretation

The lowermost (I&II) and uppermost (IV&V) units are more weathered than the laminated sequence. The question of pre-burial weathering versus *in situ* post-depositional alteration can be approached by comparing the clay spectral features, and the nature and abundance of carbonates susceptible to dissolution and reprecipitation. The samples from the basal unit (650-660) and the uppermost yellow band (093-100) that exhibit the highest clay contents are both associated with high carbonate concentrations (Fig. 4). However, carbonates in the lower units (I&II) occur as detrital largely undissolved particles as opposed to the *in situ* precipitates in the upper section (III&IV) (Fig. 6). Clay mineral formation within the laminations (II&III) is spatially restricted to traces of bioactivity and therefore took place *in situ*. Consequently, clay minerals in the lower sequence are interpreted to be primarily inherited from reworked material mixed with carbonate clasts, while throughout laminated aggradation a sizable contribution was formed *in situ* dissolving all carbonate particles in the affected zones. Carbonate and gypsum precipitation around tubular structures (weathered plant material?) is clearly evident in the 244-250 tufa-bearing yellow band. The clay mineral contents of the palaeosol and surface drape (Fig. 4) are among the lowest and largely consigned to mud aggregates (Fig. 6). Their wide range of mineral particle sizes suggests reworking of various source materials. The large primary mineral particles stand in contrast to the fine-grained homogenous bedrock specimen, but compare well with the finer fraction of the dune sample. The correlation between quartz size and abundance within the laminated sequence (II&III) possibly reflects palaeo-wind speeds in a scenario in which quartz sand, as the dominant dune mineral constituent, would have been winnowed from upwind dunefields.

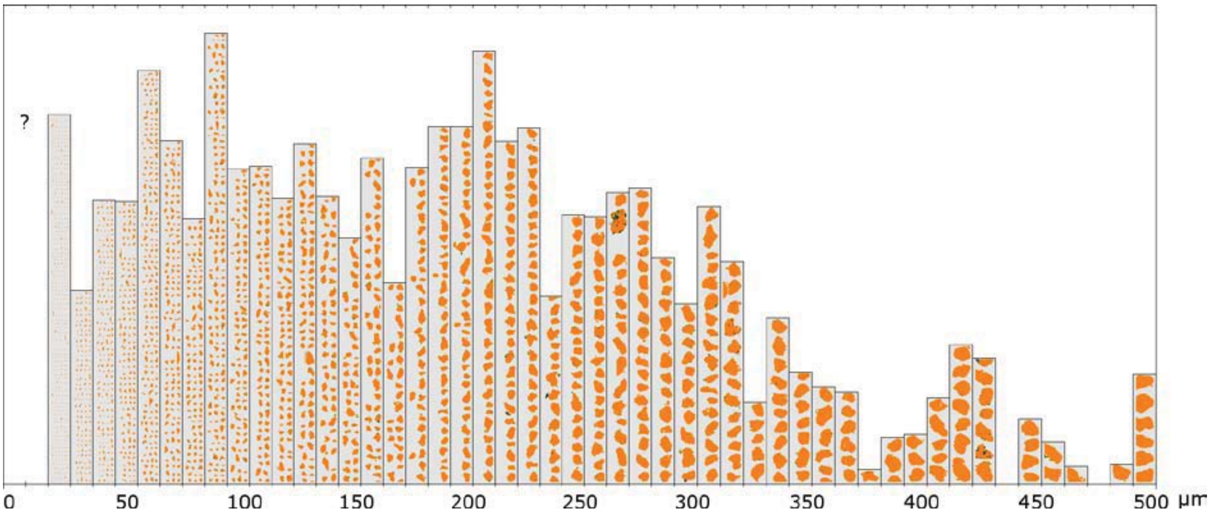

Fig. 6) QEMSCAN® field scans: *mineral maps of the undisturbed polished sample specimens. The 10 most abundant minerals are colour-coded against the white background (see legend). A graphic scale is presented in form of maximum silt-, very-fine sand-, and sand-sized particle diameters (Wentworth*

classification). Key features discussed in the text are pointed out by annotated yellow markers: ***a)*** *sand-sized well-rounded quartz and K-feldspars;* ***b)*** *mud-aggregates composed of fine sand, silt and clay particles;* ***c)*** *lithic sand and gravel;* ***d)*** *unaltered detrital clasts of carbonate;* ***e)*** *trace fossils/channels filled and lined by secondary clay minerals;* ***f)*** *in situ carbonate/gypsum/iron oxide precipitation around tubular voids; and,* ***g)*** *iron oxide-cemented plant pseudomorphs.*

Magnetostratigraphy

Sedimentary deposits such as loess/palaeosol sequences (Heller and Liu, 1984) and loess-derived slackwater aggradation (Huang et al., 2007) record vertical trends in measured variations in magnetic susceptibility that reflect climate and sediment unit-specific information (Maher, 1998). Magnetic susceptibility (κ) is defined as the magnetisation (M) of the sediment material by an induced magnetic field (H), both measured in amperes per metre; $\kappa = M/H$. The degree of magnetisation induced by the applied magnetic field is related to the mineralogy and particle-size distribution of constituent iron oxides. There is little if any correlation between total iron content and magnetic susceptibility (Fine et al., 1995) because the strong ferrimagnets magnetite (Fe_3O_4) and, by subsequent oxidation, maghemite (γFe_2O_3) that dominate measured soil magnetic remanence and susceptibility occur only in trace amounts (Maher, 1998). Loess may also have a weak susceptibility component from hematite and goethite (Zhou et al., 1990). Significant magnetic enhancement may result from pedogenic formation of ultra-fine magnetite or maghemite, biogenic contributions (bacterial Fe_3O_4), or burning of the (vegetated) surface producing trace amounts of ultrafine ferromagnetic minerals. Pedogenic formation of ferrimagnets is favoured in well-drained soils while prolonged waterlogging results in iron reduction and magnetic depletion by favouring the formation (conversion) of weakly magnetic Fe^{3+} sulphides or by dissolution (Maher, 1998). The magnetostratigraphy of the section can therefore be interpreted as a proxy for the degree of pedogenesis experienced, the hydrological history of the site, or in terms of clastic magnetic mineralogy and/or the concentration of magnetic minerals.

Protocol

The Bartington Instruments MS2® Magnetic Susceptibility System was employed in conjunction with the MS2E sensor with a probe area of 3.8 mm x 10.5 mm designed to perform high-resolution volume susceptibility measurements on the surface of cores (Bartington, 2007). The sensor was moved incrementally in 1 cm intervals along the full length of the air-dried surface of overlapping section cuttings (obtained from the cleaned section face by P.G. using an angle grinder), and calibrated with a standard between each reading. The process was repeated three times across different transects offset from the central line, and mean and median values were plotted (Fig. 7).

Results

The depth plot of measured magnetic susceptibility values shows considerable variation between individual readings, but also indicates major trends. The sequence can be subdivided into three segments, largely corresponding with the stratigraphic units I, II&III, and IV/V, based on susceptibility values above and below 10^{-4} SI units (Fig. 7). The basal unit (I) is marked by elevated values (mean = 12.3 x 10^{-5} SI) decreasing towards the palaeosol. One narrow band of values that falls below 10 x 10^{-5} SI correlates laterally with the sheet of tufa clasts and small pebbles (Photo 1). A significant change is recorded with the onset of laminated aggradation (II&III), with susceptibility values fluctuating around a mean of 5.8 x 10^{-5} SI. Depleted values coincide with bands characterised by *in situ* tufa formation, most pronounced in the transitional unit (II) and the 244-250 tufa-bearing yellow band. Above the last discernible organic veneer, susceptibility values rise (mean = 14.4 x 10^{-5} SI) throughout the pedogenic unit (IV), with a dramatic increase (mean = 81.3 x 10^{-5} SI) towards the surface drape (V). The ratio of 2.6 between the elevated units (I&IV) and the laminated sequence (II&III) is identical to the ratio between 178 palaeosol samples and 227 pristine loess samples calculated for the Chinese loess deposits (Heller and Liu, 1984). While caution must be exercised interpreting individual readings which can be influenced by the uneven surface of the continuous section cutting and small scale mottles, the three independent readings correlate strongly with a Pearson coefficient of r=0.9.

Data interpretation

The magnetostratigraphy correlates closely with the lithostratigraphy. The magnetic susceptibility data can be interpreted in terms of: **1)** elevated values against a background indicative of pedogenic activity in well-drained soils; and, **2)** depleted values indicative of site-specific waterlogging. Accordingly, the basal (I) and the upper units (I&IV) are both characterised by soil formation processes, with one important distinction: while the uppermost Bca-horizon records a sharp increase towards the top of the section, the lower unit records a gradual decrease towards the top of the palaeosol. This can be explained by assuming that the lower sequence (I) consists of reworked sediments. During the erosion of former floodplain remnants and/or valley slope mantles, soil horizons with the highest susceptibility values are likely to become redeposited first. Alternatively, the susceptibility decrease could reflect the exposure of the palaeosol to stagnating water. In the overburden, a change in sediment supply relating to the influx of “pristine” loess is recorded. Pronounced negative excursions in otherwise relatively uniform “background” susceptibility values throughout laminated aggradation (II&III) are interpreted to reflect temporal waterlogging. Bands of depleted values are often associated with paludal tufa, interpreted to have formed in ponding conditions that by modern analogy must have lasted for weeks. The exceptionally high values towards the surface drape (V) can be explained by the assumption that the material was recycled between creek beds and floodplain, reflecting multiple iron reduction/oxidation cycles (Haberlah et al., in press).

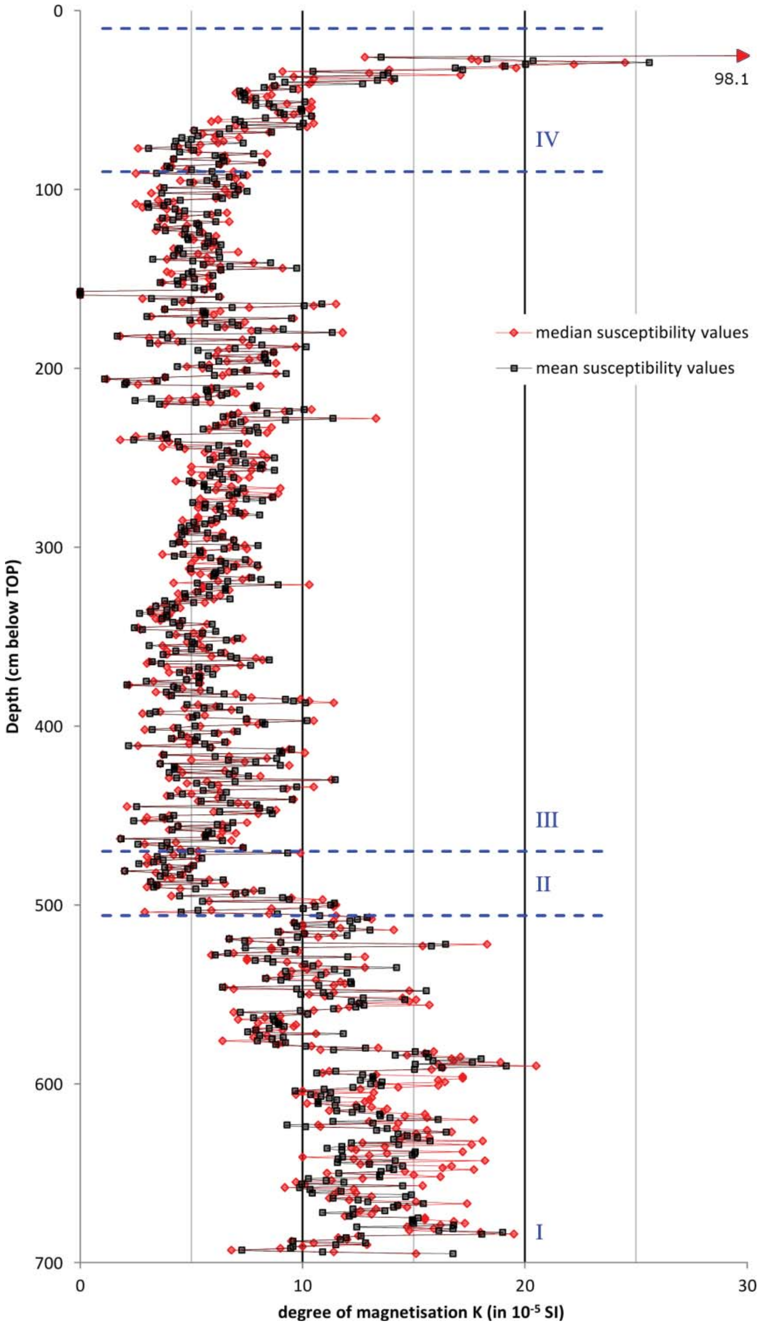

Fig. 7) Magnetic susceptibility log: *mean (black) and median values (red) of three repeated magnetic susceptibility readings at 1 cm increments plotted against depth in the stratigraphic type section. Towards the surface drape (V), the values increase markedly, cumulating in 98.1 SI as indicated by an arrow. Boundaries between the main lithostratigraphic units are projected in blue.*

Carbon isotopic geochemistry

Trends in carbon isotope ratios of detrital plant matter preserved in sediment sequences record changes within the palaeo-floral composition of the catchment. Aside from a few succulents and epiphytes, terrestrial plants fix atmospheric CO_2 using two distinct photosynthetic pathways expressed by characteristic isotopic fractionation and ratio of depletion of ^{13}C (Farquhar et al., 1989). Each group, the so-called C_3- and C_4-plants, can be distinguished by a mutually exclusive range of $\delta^{13}C$-values (Marshall et al., 2007). In a recent study, the isotopic composition of plants of the Lake Eyre region flanking the Flinders Ranges to the north was measured (Johnson et al., 2005). The C_3-plants comprise all trees, shrubs, dominant chenopods and forbs, and the C_4-plants all the grasses, herbs and a few sedges. The average $\delta^{13}C$-values for these C_3-plants (-26.8 ± 1.8 ‰) and C_4-plants (-13.8 ± 0.8 ‰) are here used as endmembers in a regional isotope mass balance model. The relative percentage of the C_3-plant composition can be calculated as follows:

$$\text{C3 composition (in \%)} = \frac{(\text{Corg sample} \quad - \text{C4 endmember})}{(\text{C4 endmember} - \text{C3 endmember})} * 100$$

with "C_{org} sample" referring to the measured $\delta^{13}C$-values of the analysed veneers of organic detritus and pieces of charcoal expressed in ‰ relative to the Peedee Belemnite Standard (PDB). The isotopic composition of sampled bulk organic matter is interpreted to reflect the relative C_3/C_4-plant abundance in the Brachina catchment at the time of entrainment and deposition in the aggradational sequence. Preferential incorporation and/or preservation of C_3- versus C_4-plants in organic debris, with the potential to systematically offset the equation, is addressed by analysing a representative (~200 g) sample of flotsam collected on-site in the aftermath of the once-in-a-hundred-years flood that occurred in January 2007. The model does not take into account any post-depositional modification of the isotopic signatures. However, significant alteration by biogenic activity and pedogenesis is unlikely given the excellent preservation of the fragile organic veneers. Contributions of aquatic plants such as phytoplankton and macrophytes cannot be ruled out, but the reported range of $\delta^{13}C$-values, particularly throughout laminated aggradation, is too small and isotopically enriched for such a scenario (Leng et al., 2006; Finlay and Kendall, 2007). The palaeo-floral composition of C_3- and C_4-plants is the product of global, regional and local meteorological and climatic controls. The C_4 photosynthetic pathway is favoured by low atmospheric pCO_2, high water stress and high temperature (Ehleringer et al., 1997; Sage and Coleman, 2001). Trees and other higher C_3-flora are less efficient in water use and do not recover as easily from wildfires (Tipple and Pagani, 2007). The sensitivity of C_3- and C_4-plants towards temperature changes and water stress is also a function of the seasonal rainfall regime (Liu et al., 2005; Finlay and Kendall, 2007). For a given

pCO_2, cooler, wetter conditions favour C_3-plants, while warmer, more arid conditions favour C_4-plants.

Protocol

Several grams of bulk organic matter, targeting every discrete veneer and piece of charred vegetation, were collected from the continuous section cutting and across the full section face. The samples were pulverised, then acidified several times in 1 m HCl to remove carbonates, rinsed twice in deionised water, dried and weighed into tin capsules. All samples were run by continuous flow on a Fisons Optima stable isotope-ratio mass spectrometer coupled to a Fisons elemental analyser. Sample data were corrected for internal fractionation during each run based on the measured values of regularly spaced standards whose isotopic compositions bracketed those of the samples. Multiple house standards were measured during each analytical run to ensure consistent reproducibility, which was 0.6 ‰ (1σ; n=13) over the course of the analyses. Duplicates were measured on more than 10 % of the samples as an additional assurance of sample reproducibility.

Results

The samples from the section cuttings (grey triangles) comprise the 32 best-developed and most continuous organic veneers from the laminated sequence (II&III) (Fig. 8). An additional 58 samples extend and complement this record by including more disturbed and partly discontinuous veneers, detrital charcoal from the basal unit (I) and lower yellow bands (II), and modern flotsam (black triangles). One third of those samples (19, white triangles) were also sent to The Australian National University (ANU) for radiocarbon dating on the Single Stage Accelerator Mass Spectrometer (SSAMS), which reports the precision of the $^{13}C/^{12}C$ ratio within 2 ‰ (Fifield et al., 2007). The pre-treatment for radiocarbon dating involved alkaline leaching of humic acids with the aim to concentrate the insoluble charred organic fraction (Olsson, 1986). The $\delta^{13}C$-values associated with the isolated plant fractions exceed the range of values reported for the bulk organic matter (Fig. 8), and were excluded from the following calculations.

With an average $\delta^{13}C$-value of -23.6 ‰, the material sampled from the basal unit (I) reflects a predominant C_3-plant composition (>75 %). The onset of laminated aggradation (II) coincides with a marked shift in the palaeo-floral composition towards C_4-grasses at the expense of C_3-plants, declining from -26.4 ‰ (93 %) to -20.2 ‰ (<50 %) just above the 470-479 red band. Subsequently, the strongly fluctuating $\delta^{13}C$-values become, on average, more ^{13}C-depleted towards the uppermost laminations, reaching -22.3 ‰ (65 %) at 169 cm. This overall trend marking the laminations can be subdivided into a lower part, characterised by an average $\delta^{13}C$-value of -22.0 ‰ corresponding to a 63 % C_3-plant contribution reaching a plateau at ~320 cm, with values decreasing from -22.1 ‰ – -

24.2 ‰, and an upper part, with an average of -22.7 ‰ corresponding to a 68 % C_3-plant abundance terminating in a plateau at 169 cm, with values increasing from -20.9 ‰ – -23.4 ‰. The uppermost sequence (IV), hosting only a few poorly-preserved organic veneers that terminate by 51 cm depth, reflects an increase in C_3-plants with an average δ^{13}C-value of -23.1 ‰ translating to a C_3-plant contribution of 72 %. Finally, the δ^{13}C-value of -26.8 ‰ obtained from present-day flotsam suggests a 100 % C_3-plant composition.

Data interpretation

While small-scale fluctuations in δ^{13}C-values may reflect short-term variations in the palaeo-floral composition, the larger scale plateaus at the onset of laminated aggradation at 506 cm, and just below 300 cm, are best explained within a chronological context. Calibrated radiocarbon ages of concentrated C_3-plant fragments (charcoal) predate those of concentrated C_4-plant fragments, invariably returning pre-24 ka cal BP ages for the lower half of the laminations (Fig. 8). Hence, these isotopically depleted vegetation elements predate the laminated depositional regime, representing sequestered residual and possibly reworked charcoal. Reworking is also envisaged for C_3-plant material dominated samples from the basal unit (I) that are older than the lowermost radiocarbon age, i.e. within the range of ~34-29 ka cal BP. If so, the Brachina catchment is characterised by a relatively C_4-dominated floral composition throughout the lead-up and peak of the LGM, with a fluctuating but overall continuous increase in C_3-plant contribution to the total sedimentary organic carbon. C_3-vegetation possibly prevailed during peak glacial conditions ~320 cm, but still remained ~20 % below the isotopic composition of modern flotsam. Considering the sizeable quantity of C_3-grasses growing within the catchment today, the 100 % C_3-plant equivalent δ^{13}C-value from the collected modern organic debris suggests that transport and depositional processes and/or organic decay systematically discriminate against C_4-plants in flotsam, possibly reflecting the higher preservation potential of lignin and cellulose which is more significant in C_3-plants. The relative predominance of C_4-plants throughout the LGM despite prevailing lower temperatures cannot be explained by the lower pCO_2 alone, but rather indicates seasonally and inter-annually more arid conditions and possibly more frequent wildfires.

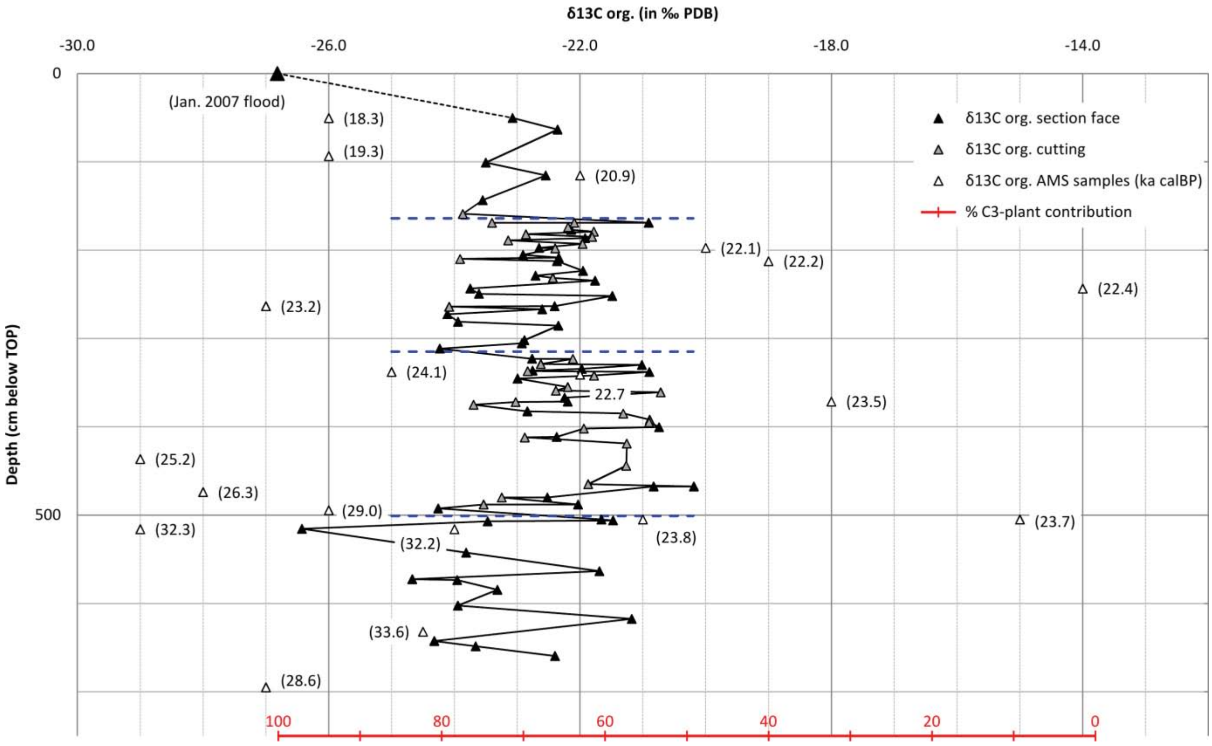

Fig. 8) Carbon isotopic log: *δ^{13}C-values of bulk organic matter plotted against depth in the stratigraphic type section. Samples collected from the section face are presented in black, samples from the continuous section cuttings in grey, and dated sub-samples in white listing their corresponding ^{14}C-ages in ka cal BP. The lower abscissa presents their relative percentage of C_3-plant contribution according to regional isotope mass balance model based on data from Johnson et al. (2005). Plateaus in δ^{13}C-values discussed in the text are projected in blue.*

Chronostratigraphy

In order to establish the timing and rates of deposition of the main stratigraphic units, 33 age estimates were obtained: 27 by accelerator mass spectrometry (AMS) radiocarbon dating, and 6 by optically stimulated luminescence (OSL) dating. Within the radiocarbon dating program, three types of organic materials were sampled from the section: discrete charcoal pieces, bulk plant detritus from organic veneers, and intact freshwater gastropod carbonate shells. The fundamental principle behind radiocarbon dating is that the radioactive isotope ^{14}C decays at a constant rate from an initial concentration in near-equilibrium with a known atmospheric concentration starting with the death of the organism (i.e. cessation of photosynthesis or the intake of biomass) (Bowman, 1990). Hence, ^{14}C-dating of charcoal establishes the age of cell growth, ^{14}C-dating of organic veneers averages the time of death of plant litter (and charcoal) entrained by the flood event, and ^{14}C-dating of carbonate shells reflect the age of carbonate precipitation. None of these are necessarily coeval with the depositional event, as demonstrated in a study on contemporaneous charcoal in a fluvial environment by Blong and Gillespie (1978). The relative resilience and longevity of charcoal make it prone to endure multiple cycles of erosion and redeposition. The same principle applies to shells and plant litter, albeit perhaps to a lesser degree considering their relative fragility. Therefore, ^{14}C-ages must be strictly treated as terminus post quem in any chronostratigraphic context. The OSL-ages date the timing when the sampled subset of quartz grains were last exposed to light prior to burial and consequent irradiation (Aitken, 1998). The timing of exposure can vary from grain to grain, particularly if the sediment only experienced short-distance transport with high suspension load concentrations (Olley et al., 1998). Post-depositional contamination by infiltration of “younger” grains by seepage, pedogenesis or bioturbation further complicates the analysis. With recent technical advances in luminescence readers, dating protocols and age models, these can now be accounted for on a grain by grain basis (Duller, 2004). However, a decade ago when the OSL-ages for BRA-SD were analysed, the luminescence signal could only be averaged across large aliquots of grains mounted on 1 cm discs (see Williams et al., 2001 for details).

Protocol

Radiocarbon samples were pre-treated, the carbon extracted and converted to graphite using standard methods (Hua et al., 2001). The samples were either dated on the ANTARES AMS facility at ANSTO (Fink et al., 2004) (code: OZJ), or the recently installed SSAMS at the ANU (Fifield et al., 2007) (code: SSAMS). In addition, two previously published AMS-ages (Cock et al., 1999) (code: Beta) are included in the discussion and, like the other samples, calibrated using the integrated CalPal-2007$^{\text{Hulu}}$-calibration data set (Weninger and Jöris, 2008), as part of the CalPal-2007 calibration and palaeoclimate research software package (Weninger et al., 2008).

Results

The independent age proxies allow quantification of the material-dependent residual times, best demonstrated by plotting age, sample material and method versus depth in the section (Fig. 9). In comparison to the calibrated AMS-ages, the OSL-ages appear to be younger by 2-3 ka (Table 1). AMS-ages based on both charcoal and shells, and OSL-ages describe a marked age inversion in the basal unit (V); from ~27-28 ka cal BP (assuming a systematic offset in the OSL data) via ~32-36 ka cal BP back to ~26 ka cal BP (OZJ909). Layered to laminated aggradation (II&III) sets in ~24 ka cal BP with the lowermost veneer of organic detritus dated to 23.83 ± 0.25 and 23.71 ± 0.20 ka cal BP (SSAMS ANU 4117, 4205). Large discrepancies between individual AMS-ages are apparent during the onset of the laminations. All discrete charcoal pieces (SSAMS ANU 2030, 2035) and the gastropod shell (OZJ905) sampled from yellow bands return ages a few thousand years older than those from corresponding organic veneers, suggesting reworking and long residence times of the material within the catchment. Fragments of residual charcoal are also incorporated in some of the lower organic veneers. By using the reported $\delta^{13}C$ data and the regional isotope mass balance model (Fig. 8), a division was made into predominantly woody charred C_3-plants, likely to survive multiple cycles of erosion and deposition, and the more fragile C_4-plant-rich detritus (>-24 ppm PDB, <80 %), sensitive to such reworking (Fig. 9). The latter samples display a coherent age-depth trend throughout the laminated profile, with a linear regression suggesting a depositional rate of ~83 cm/ka (r=0.95). In contrast to the onset of layered to laminated aggradation, C_3-plant based ^{14}C-ages associated with the termination (IV) appear contemporary with the depositional events. Accordingly, a marked reduction in depositional rates to ~23 cm/ka (r=1) set in as early as ~22 ka cal BP (SSAMS ANU 4206) with layered to laminated aggradation terminating at 18.28 ± 0.23 ka cal BP (SSAMS ANU 4107).

(see opposite page)

Table 1) BRA-SD radiocarbon ages: *Accelerator mass spectrometry (AMS) radiocarbon data listed by sample material: C_4-plants refer to bulk organic matter with $\delta^{13}C$ values >-24 ‰, C_3-plants to $\delta^{13}C$ values <-24 ‰, and $CaCO_3$ shells relate to unbroken carbonate shells of freshwater gastropods. All samples are correlated in depth to the stratigraphic type section (see appendix 5.3A). The ^{14}C-ages are calibrated using the integrated CalPal-2007^{Hulu}-calibration data set (Weninger and Jöris, 2008), as part of the CalPal-2007 calibration and palaeoclimate research software package (Weninger et al., 2008).*

Lab code	**Sample material**	**below TOP** (in cm)	**Age** (in ka BP)	**Error** (1 SD)	**Age** (ka cal BP)	**Error** (1 SD)	**δ13C** (in ‰)
SSAMS ANU 4207	C_4-plants	**116**	17.42	*0.12*	**20.92**	*0.17*	-22
SSAMS ANU 4206	C_4-plants	**198**	18.41	*0.10*	**22.11**	*0.25*	-20
SSAMS ANU 4110	C_4-plants	**213**	18.52	*0.12*	**22.23**	*0.26*	-19
SSAMS ANU 4111	C_4-plants	**244**	18.61	*0.13*	**22.41**	*0.18*	-14
SSAMS ANU 4114	C_4-plants	**341**	18.88	*0.14*	**22.68**	*0.15*	-22
SSAMS ANU 4209	C_4-plants	**372**	19.67	*0.12*	**23.54**	*0.12*	-18
SSAMS ANU 4117	C_4-plants	**505**	19.82	*0.18*	**23.71**	*0.20*	-15
SSAMS ANU 4205	C_4-plants	**505**	19.91	*0.18*	**23.83**	*0.25*	-21
SSAMS ANU 4107	C_3-plants	**51**	15.16	*0.10*	**18.28**	*0.23*	-26
SSAMS ANU 4109	C_3-plants	**94**	16.17	*0.12*	**19.34**	*0.20*	-26
SSAMS ANU 4112	C_3-plants	**264**	19.36	*0.14*	**23.23**	*0.15*	-27
SSAMS ANU 4113	C_3-plants	**338**	20.13	*0.16*	**24.08**	*0.24*	-25
SSAMS ANU 4116	C_3-plants	**437**	21.12	*0.15*	**25.16**	*0.24*	-29
SSAMS ANU 2030	C_3-plants	**474**	21.89	*0.16*	**26.26**	*0.31*	-28
SSAMS ANU 2035	C_3-plants	**495**	24.11	*0.21*	**28.99**	*0.39*	-26
SSAMS ANU 2036	C_3-plants	**516**	27.63	*0.28*	**32.21**	*0.26*	-24
SSAMS ANU 2037	C_3-plants	**516**	27.74	*0.29*	**32.31**	*0.29*	-29
Beta-96679	C_3-plants	**565**	29.80	*0.18*	**33.56**	*0.30*	-
OZJ904	C_3-plants	**632**	29.16	*0.38*	**33.57**	*0.41*	-25
SSAMS ANU 2039	C_3-plants	**695**	23.60	*0.30*	**28.56**	*0.42*	-27
OZJ905	$CaCO_3$ shell	**353**	20.46	*0.14*	**24.45**	*0.19*	-
OZJ909	$CaCO_3$ shell	**508**	21.51	*0.31*	**25.66**	*0.46*	-
Beta-96166	$CaCO_3$ shell	**565**	28.12	*0.16*	**32.57**	*0.26*	-
OZJ908	$CaCO_3$ shell	**639**	27.99	*0.71*	**32.64**	*0.63*	-
OZJ907	$CaCO_3$ shell	**667**	27.32	*0.28*	**31.97**	*0.20*	-
OZJ906	$CaCO_3$ shell	**684**	27.20	*0.50*	**31.9**	*0.39*	-
SSAMS ANU 1811	$CaCO_3$ shell	**695**	23.27	*0.09*	**28.08**	*0.08*	-

Data interpretation

By increasing the resolution and variety of dated samples, a more detailed but also more complex chronostratigraphic picture emerges than previously assumed (Williams et al., 2001). Irrespective of sample type and dating method, the basal unit (I) displays a marked age inversion best explained by incorporation of reworked older material. The coincident poorly-bleached OSL sample AdGL-96003, and the unbroken condition of the large pieces of charcoal and shells suggest short-distance transport, possibly from adjacent valley slope mantles or nearby remnants of a former floodplain. While a tentative hiatus lasting for ~2 ka between deposition of the palaeosol sediments and the onset of the laminations can be inferred from shell sample OZJ909 obtained from the uppermost palaeosol, further dating by means of single-grain OSL-age estimates is required. Laminated aggradation setting in ~24 ka was rapid with close to four metres of deposition prior to peak LGM conditions ~21 ka. Significant amounts of residual charcoal and the occasional shell were initially sequestered with the coarsest suspension load (yellow bands). Organic veneers topping a closely spaced succession of yellow bands (SSAMS ANU 4111, 4110, 4106) indicate episodic aggradation, possibly of centennial frequency. The second half of the LGM experienced a marked reduction in deposition rates, and an increase in what appears to be contemporary elements of C_3-plants. Fine-grained aggradation terminated towards the end of the LGM ~18 ka. The surface drape remains to be dated.

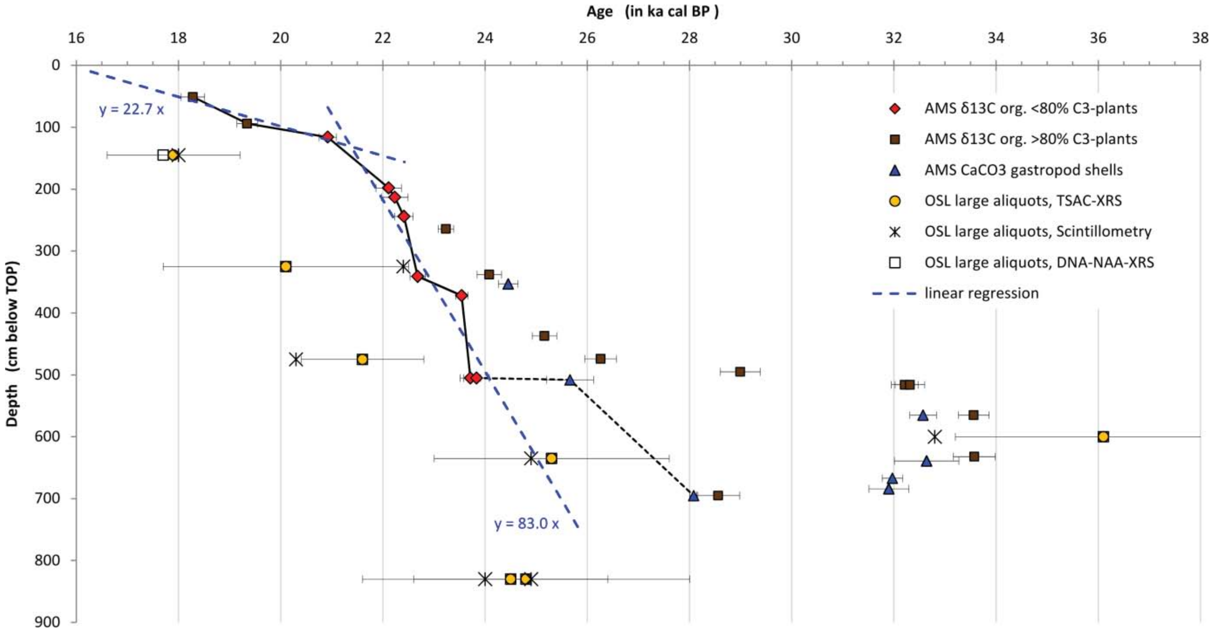

Fig. 9) BRA-SD age-depth plot: *accelerator mass spectrometry (AMS) radiocarbon data (see Table 1) are plotted as calibrated ages with error bars and colour-coded by sample material. Based on the regional isotope mass balance model generated from data published in Johnson et al. (2005), the*

bulk organic matter is divided into predominantly woody C_3*-plants (*$\delta^{13}C$ *<-24 ‰), including all discrete charcoal pieces depicted as brown squares, and organic detritus composed largely of* C_4*-plants (*$\delta^{13}C$ *>-24 ‰) depicted as red diamonds. Dated carbonate shells from unbroken freshwater gastropods are depicted as blue triangles. In addition, OSL-ages based on three independent assessments of the environmental dose rate (see Williams et al., 2001) are plotted. Two interpreted depositional rates (linear regressions) are indicated in blue and listed. AMS-ages discussed as most likely approximations of the depositional events are connected by a black line, dotted in the lower part to express increasing uncertainty.*

Discussion

The layered to laminated stratigraphic section consists principally of coarse and fine silt-sized quartz, feldspars and carbonate particles, differing in their degree of sorting and weathering. A significant segment of the primary minerals are larger than those in the fine-grained homogenous shales that underlie the sequence and most of the upstream valley-fills. The full size range of the sediments can be found in dune sands extending from playa Lake Torrens towards the range front. The apparent size dependency of the quartz abundance in the laminated sequence is consistent with the inferred **aeolian provenance** of the material, with quartz content and its mean particle sizes increasing simultaneously as more and larger material is entrained and transported from the quartz-dominated dunefields by strong westerly winds. Winnowing of active dunefields is suggested as a source for well-studied glacial loess (Sun et al., 2002) and desert loess (Crouvi et al., 2008) occurrences, and provides a plausible provenance scenario for the similar Namib Silts (Eitel et al., 2001) and Sinai Silts (Rögner et al., 2004).

The presence of rolled detrital pedogenic carbonates, clasts of tufa, lithic sand and gravel, and traces of current cross-bedding indicate that the **basal unit (I)** aggraded as fluvial bedload. The alternating, upward-thinning lighter and darker bands are interpreted as a sequence of flood couplets decreasing in thickness towards the palaeosol. The darker bands, including the palaeosol, inherited some of their colour from plant detritus, in places still preserved as discontinuous veneers. The decreasing thickness of the couplets possibly reflects an increasingly limited sediment supply and/or an increase in accommodation space as the bedrock topography of narrow rock-cut channels became filled in. The results of the mineral spectroscopy show that the basal unit (I) is rich in secondary clay minerals indicative of chemical weathering, an interpretation consistent with the magnetic susceptibility record. The hematite- and goethite-masked (red-brown) colour of the sediments and the presence of undissolved detrital carbonate particles and shells suggest that the material consists of reworked well-aerated former floodplain remnants and/or valley slope mantles. This scenario is consistent with paired AMS- and OSL-age inversions, indicating inherited ages for material dated ~36-32 ka, with fluvial redistribution setting in ~28 ka cal BP or earlier.

The 506-516 cm **palaeosol,** as the uppermost and best-defined darker band, marks a hiatus followed by a pronounced shift in the depositional environment. In terms of bulk mineralogy, overall particle-size distribution, poor sorting and the presence of mud aggregates and large well-rounded sand grains, the palaeosol presents a buried analogue of the present surface drape. However, there are discrepancies between the two: **a)** the dark brown/grey colour of the palaeosol versus the yellowish red colour of the surface drape, **b)** the blocky to prismatic structure with slickensides versus a granular to platy structure, and **c)** induced magnetic susceptibility values that decrease towards the top of the palaeosol but sharply increase towards the top of the section. These differences can perhaps be explained by the comparably short-lived nature of the hiatus, possibly limited to ~2 ka or less, and by the hydrological environment of subsequent deposits. Large pseudogleyic root casts that extend from above testify to the palaeosol’s inundation.

While the onset of laminated aggradation marks a sudden change in the depositional mode, redoximorphic pale and lepidocrocite-dominated (orange) colours that characterise the >4 m of laminations dominate above the **transitional unit (II)**. Inherited AMS-dated charcoal and shells are consistent with a scenario of a gradual decrease in reworked material and sequestered organic matter. The sediments of the **laminated unit (III)** above 470 cm appear to have experienced little prior weathering, with secondary mineral formations restricted to traces of roots and burial activity, and magnetic susceptibility values common for pristine loess accessions. The laminated aggradation (II&III) is characterised by an absence of coarse material, cross-bedding and erosional contacts, all indicating a low-energy depositional environment. The stacked fining-upward pattern of the laminations is interpreted to reflect the density-sensitive settling velocities of suspended sediments. The yellow bands settled out of the water column first, effectively blanketing the flooded surface as flow capacities were reduced by backflooding from the gorge entrance. Their remarkably narrow absolute size-range is interpreted to reflect: **a)** an upper particle-size range constrained by wind velocities; and, **b)** additional sorting controlled by Stokes' law. Subsequently, floating plant litter settled out with the bulk of the fine silt-sized population. Tufa formed *in situ* during desiccation. Under the present climate, similar tufa precipitates over days and weeks in pools of water lining the creek bed in the aftermath of a major flood event. The thickness of the slackwater couplets relates to the suspension load, which is a function of the magnitude of the flood event and distance from the main flow. The more discontinuous laminations record either discrete smaller-scale inundations or multiple sediment fluxes over the course of a single large-magnitude flood event (Kochel and Baker, 1988). The slackwater scenario is consistent with the increase in thickness of the yellow bands and the overall sequence downstream towards the present-day confluence with the Etina Creek. According to the gravel imbrication pattern, this channel persisted as the main axis of flow throughout the LGM, episodically inundating the peripheral depression that is now occupied by the stratigraphic section. The change in deposition from flood couplets to slackwater couplets corresponds with: **a)** a substantial increase in accommodation space as the pre-existing rock-cut channels were filled and the flow of the Brachina tributary spread out across the width of the valley; **b)** a major influx of proximal dust; and, **c)** a decrease in perennial C_3-vegetation within the catchment. Water stagnation was short-lived and penetrated only newly deposited sediments, as manifested in the unaltered state of fine carbonate particles and hematite coatings of the 470-479 red band. Bioturbation likewise was limited in duration and penetration.

In contrast, the termination of the fine-grained aggradational regime is characterised by pronounced pedogenesis and bioturbation coeval with an increase in C_3-plants. The **pedogenic unit (IV)** records a fourfold decrease in sedimentation rates and a sudden presence of gravels. This is consistent with fine sediment starvation, i.e. the final stripping of loess-mantled valley slopes and consequent headward erosion, incision and realignment of the Brachina Creek along the northern flank of the valley to its present (and possibly pre-aggradational) course. Fluvial aggradation is superseded by the aeolian/colluvial deposition of a thin **surface drape,** possibly sourced from desiccating creek beds during dust storms.

Palaeoclimatic and **palaeo-environmental** controls promoted the widespread aggradation of fines, as opposed to their erosion by ephemeral traction load streams under the current climate. Since the 1960s, “pluvial” anomalies in the overall more arid glacial landscape of south-eastern Australian are discussed as expressions of complex local hydrological responses to lower temperatures (Galloway, 1965). This minevaporal theory was invoked to explain the Brachina Silts in terms of a low-energy perennial wetland with swamp vegetation trapping dust washed in by gentle winter rainfall (Williams et al., 2001; 2006). However, reduced evapo-transpiration alone does not produce run-off capable of inundating and backflooding wide reaches of the valleys. The recently established coeval aggradation of extensive floodplains on the piedmont plain (Haberlah et al., in press) further emphasises a simple fact: flood deposits involve flooding rains.

The LGM sequence of slackwater couplets indicates that the frequency and magnitude of exceptional rainfalls was similar or even of larger magnitude from today, raising the question about the controls that determine their erosive capacity. Over an interval of relative tectonic stability

(Quigley et al., 2007), aggradation and degradation of the fluvial system are determined by discharge and erosional/transport capacity, i.e. the rate of surface run-off and sediment supply. Surface run-off is inversely related to the vegetation cover (e.g. Lancaster, 2002). The dated isotopic record of bulk organic matter from the catchment suggests that the C_3-vegetation that presently stabilises the hillslopes was burnt ~32 ka, and only recovered towards the Deglacial. The interval spanning the lead-up to and peak of the LGM was dominated by C_4-grasses, possibly reflecting the higher tolerance of the C_4-photosynthetic pathway to droughts and flooding (Baruch, 1994; Heckathorn et al., 1999). The transition from a temperate, more humid to a cold and arid climate characterised by the collapse of the perennial protective vegetation cover would have promoted valley slope erosion and, by increasing the sediment supply, an aggradational fluvial regime (Harvey and Wells, 1994; Zielhofer and Faust, 2008). The same scenario was suggested to explain palaeofloods larger in magnitude and further in reach than today depositing the lower Tsondab Silts in Namibia at ~28-26 ka and ~22-20 ka (Lancaster, 2002). In contrast, the recovery of perennial vegetation towards the end of the LGM would have favoured stream incision by reducing the sediment supply, thereby increasing the erosional capacity of the run-off (Harvey and Wells, 1994; Lancaster, 2002; Hessel, 2006). This is consistent with pollen and charcoal particle concentrations from terminal playa Lake Frome recording a marked increase in C_3-vegetation from ~20 ka over a period of low wildfire frequency (Singh and Luly, 1991; Luly and Jacobson, 2000). The deposition/erosion rates can be expected to vary along the thalweg, depending on the local topography that controls flow velocities over the passage of the flood (van Maren et al., 2009). Slackwater deposits with the potential to record discrete flood events are restricted to backflooded reaches upstream of gorges, flooded tributary mouths and protected embayments (Kochel and Baker, 1988), and were described from all of these settings from multiple catchments in the Flinders Ranges (Haberlah et al., in press). Along the main flow, lateral floodplain accretion and, with increasing transmission losses, flood-outs will dominate aggradation, possibly explaining the range of depositional interpretations by different authors that studied different sections of the Namib Silts (for reviews see Lancaster, 2002; Srivastava et al., 2006; Haberlah, 2007; Heine and Völkel, 2009).

In the case of the Flinders Silts, the fluvial response to vegetation-controlled sediment supply may have been significantly amplified by fluxes of proximal dust. Accordingly, between ~29-18 ka the slope mantles were intermittently stripped of unconsolidated loess accessions and washed into the valley as hyperconcentrated sheet floods with little erosional capacity. As long as the fluvial regime remained charged with an excess load of loess it aggraded. Consequently, aggradation/degradation of the fine-grained regime is ultimately controlled by the dust supply and, by inference, the activity of downwind dunefields. Empirical studies and conceptual models suggest that dune activation is principally controlled by thresholds in: **1)** sediment supply; **2)** the transport capacity of wind; and, **3)** stabilisation by vegetation (e.g. Lancaster, 1994; Hugenholtz and Wolfe, 2005). These variables are strongly affected by the seasonal and inter-annual precipitation regime, but remain largely indifferent to rare exceptional rainfall events. The floor of Lake Torrens was lowered more than 2 m by deflation during the last glacial, as inferred from its former surface level preserved in form of a prominent travertine structure aged ~27.4 ± 0.5 ka cal BP (Schmid, 1990). A dune remnant rising out of the deepest part of Lake Frome was dated to ~23.3 ± 0.5 ka cal BP and presents a minimum age for the last regional deflation peak (Callen, 1984). Downwind, the source-bordering Strzelecki dunefield was reactivated throughout the LGM (Fitzsimmons et al., 2007). In conclusion, fine-grained valley-fill aggradation is restricted to geological intervals when regional water levels were low enough to expose the terminal playa lake floors, seasonal/inter-annual water stress (droughts) was severe enough to significantly reduce the plant cover, and strong westerly winds prevailed at least seasonally. When the threshold of any of those is not met, the dust source is “switched off”, which soon translates into the re-establishment of the erosional capacity of the fluvial system and valley-fill/floodplain incision.

The inferred early lead-up to the LGM, with the fluvial system responding to barren erosive slopes by ~28 ka or earlier, compares well with high-resolution palynological records from westerlies-dominated New Zealand. According to the tephra marker bed-controlled terrestrial Auckland pollen record (Newnham et al., 2007a) within the same mean zonal pressure belt of westerly airflows as the central Flinders Ranges (Shulmeister et al., 2004; Figure 1), dense forest cover was reduced to its lowest levels between ~29-25.5 ka and 24-20 ka, separated only by a short-lived “mid-LGM warming”. A major transition from cool climate grass- and shrub land to a podocarp forest is recorded for ~21-19 ka (Newnham et al., 2007a). Independent palynological records (Newnham et al., 2007a; b) and moraine mapping of glacial advances (Suggate and Almond, 2005) from both the North and South Islands support the wider, possibly southern hemispheric relevance of these palaeo-environmental changes which correspond to peak global ice-levels maintained throughout ~30-19 ka (Lambeck et al., 2002).

Conclusions

The lithostratigraphic, chronostratigraphic, geochemical and geophysical data highlight different aspects of the depositional, diagenetic and hydrological history of the layered to laminated sedimentary sequence embedded within the fine-grained valley-fills upstream of the Brachina Gorge in the Flinders Ranges. Collectively, they provide new insights about the palaeoclimate and palaeoenvironment of the region throughout the lead-up and peak of the LGM. The results of high-resolution particle-size analyses and mineral spectroscopy are consistent with earlier inferences (Williams et al., 2001; Williams and Nitschke, 2005; Haberlah et al., in press) that the bulk of the fine-grained material consists of wind-blown dust. Dunefields that extend from the downwind margin of Lake Torrens towards the Ranges are identified as a potential source, holding significant quantities of dust and silt from the deflated playa lake floor and the coalescing alluvial fans. In accordance with the chronostratigraphy, large quantities of proximal dust were deposited into the Brachina catchment in the lead-up to ~32 ka and ~21 ka, two ages correlating closely with the first-order dust peaks in the high-resolution continental distal dust record, interpreted as cold dry events or stadials (Petherick et al., 2008). The ~32 ka dust peak is preserved within the lower sequence, which, according to lithofacies observations, bulk mineralogy and induced magnetic susceptibility, experienced advanced weathering in a comparably well-aerated temperate environment. A separate regional chronostratigraphic study on the Flinders Silts concluded that the interval between ~36-30 ka is marked by calcareous pedogenesis coinciding with fluvial incision. For the interval between ~29-25 ka widespread erosion and reworking were inferred (Haberlah et al., in press). The sediments in the stratigraphic section are interpreted to be reworked and flushed into the pre-existing rock-cut channel from ~28 ka (or earlier). An interval of relative surface stability, lasting for up to ~2 ka prior to ~24 ka, marks the transition from poorly-sorted flood deposition to cyclic upward-fining slackwater deposition, with rapid aggradation rates (~80 cm/ka) throughout the first half of the LGM. Elsewhere within the floodplain, this interval is characterised by a realignment of the drainage pattern, accommodating the ~21 ka dust influx filling in the rugged topography to a point where sediment-charged floods migrated laterally across the width of the valley. A dozen large-scale and numerous smaller flood events are recorded in the form of extensive sheets of suspension fall-out. Their redoximorphic colours reflect a cool, temporarily stagnating weathering environment. The excellent state of preservation of the laminations and the hematite-masked band with undissolved carbonate particles suggests that inundation events and bioturbation were short-lived and limited to the uppermost centimetres of the aggrading sediments. The second half of the LGM is marked by a decrease in sedimentation rates (~20 cm/ka), terminating with an influx of gravel at ~18 ka. Bioturbation and pedogenesis have blurred the laminations of the uppermost metre into more transitional light and dark bands. Termination of fine-grained deposition at ~18 ka is synchronous for all valley-fills across multiple catchments in the Flinders Ranges (Haberlah et al., in press).

The fine-grained valley-fill formations in the Flinders Ranges are here interpreted as the fluvial response to glacial aridity-induced dust deposition and devegetation. Consequently, the Brachina slackwater deposit presents a proximal equivalent to regional marine and continental terrestrial distal dust records spanning the LGM (Revel-Rolland et al., 2006; Petherick et al., 2008; 2009). Heightened glacial aridity and dust storms are here shown to have coexisted with large-magnitude floods. As an alternative to linking the termination of the fine-grained aggradational regime to an inferred assumption of higher intensity rainfalls (Williams et al., 2001), fine sediment starvation over the course of Deglacial revegetation of dunes and valley slopes, and rising regional groundwater levels covering the terminal playa lake floors is suggested. More information on the source and season of the precipitation regime controlling vegetation growth and generating floods must be obtained by future research. However, the present study of one continuous sedimentary sequence has confirmed the complex environmental response to climatic variability that characterised the LGM and the times immediately before and after it, as recently outlined by other authors for Africa and Australasia (Gasse et al., 2008; Williams et al., 2009).

(see opposite page)

Photo Plate 1) *View of the vertical outcrop of stratigraphic section BRA-SD (S 31.33730°/E 138.60655°, TOP 338.1 m a.s.l.) looking upstream towards the vegetated valley slope. The five lithostratigraphic units (basal unit I, transitional unit II, laminated unit III, pedogenic unit IV, and surface drape V) are indicated and juxtaposed with the stratigraphic type section. On the section drawing, 12 lithofacies are differentiated (see legend).*

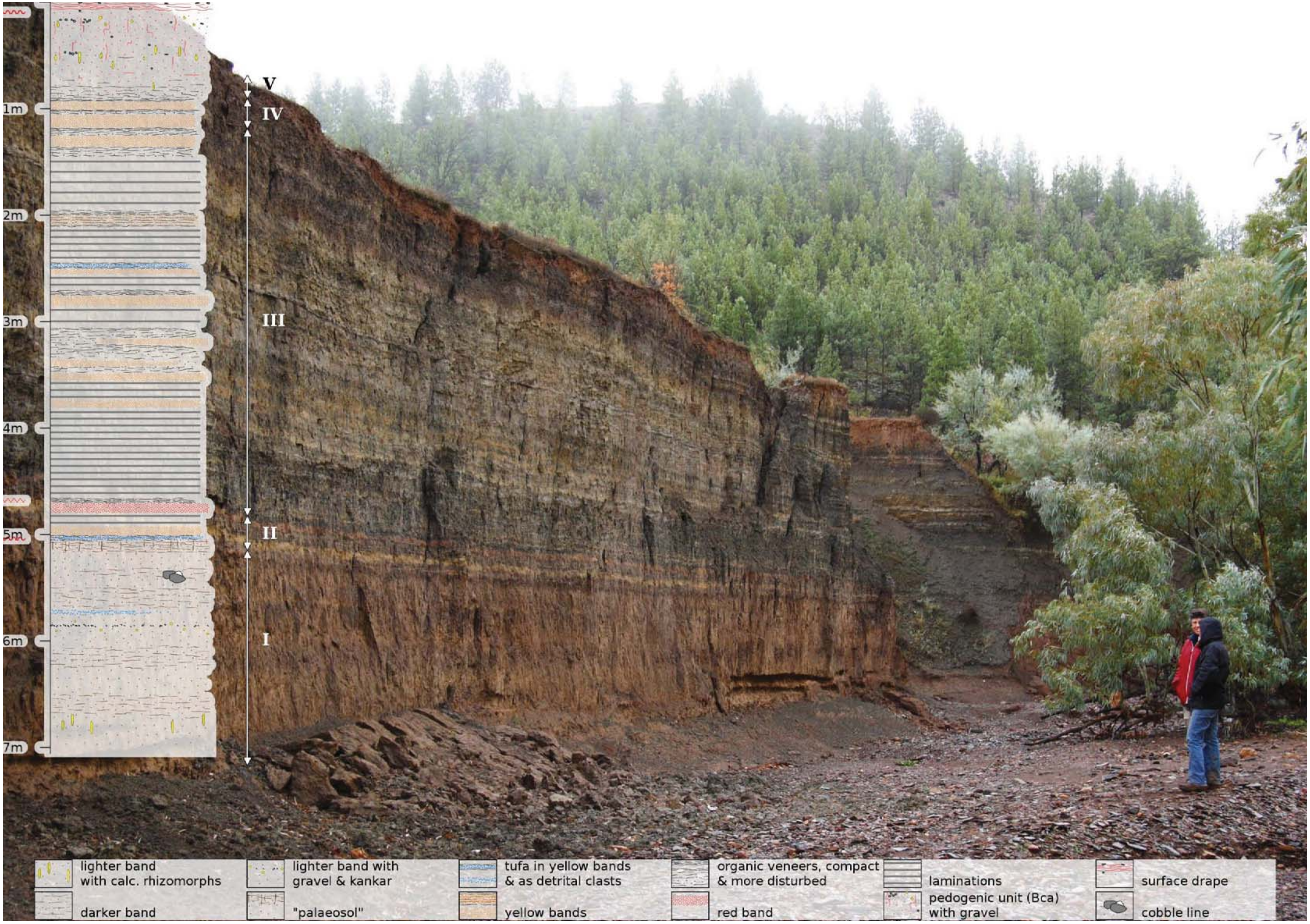
1m
2m
3m
4m
5m
6m
7m
V
IV
III
II
I
lighter band with calc. rhizomorphs
darker band
lighter band with gravel & kankar
"palaeosol"
tufa in yellow bands & as detrital clasts
yellow bands
organic veneers, compact & more disturbed
red band
laminations
pedogenic unit (Bca) with gravel
surface drape
cobble line

(see opposite page)

Photo Plate 2) *Section details:* ***A)*** *downstream end of stratigraphic section BRA-SD unconformably resting on the Neoproterozoic Brachina Shale Formation;* ***B)*** *detrital pedogenic carbonate nodules, reworked from former Bca-horizons and deposited as discontinuous sheets throughout the basal unit (I);* ***C)*** *large (8x2 cm) piece of charred wood dated to ~32.5 ka cal BP (OZJ904);* ***D)*** *narrow line of well-rounded cobbles and large clasts of spring tufa within the basal unit (I) below the palaeosol;* ***E)*** *vertical in situ calcareous rhizomorphs excavated by recent floods at the base of the stratigraphic section;* ***F)*** *pseudogleyic root cast extending from the transitional unit (II) into the basal unit (I). Stagnating surface water infiltrated the root channels leaching the soluble* Fe^{2+}*-ions which in contact with trapped soil air precipitated as orange lepidocrocite-dominated zones. The void left by microbial decomposition is filled by material similar in colour to the 470-479 red band;* ***G)*** *tufa precipitation in an evaporating pool of water after a 100-year flood in January 2007 observed in Hookina Creek to the SW. Similar tufa crust protected underlying veneers of organic flotsam from erosion by subsequent flood fluxes, with new material infiltrating into the loose structure.*

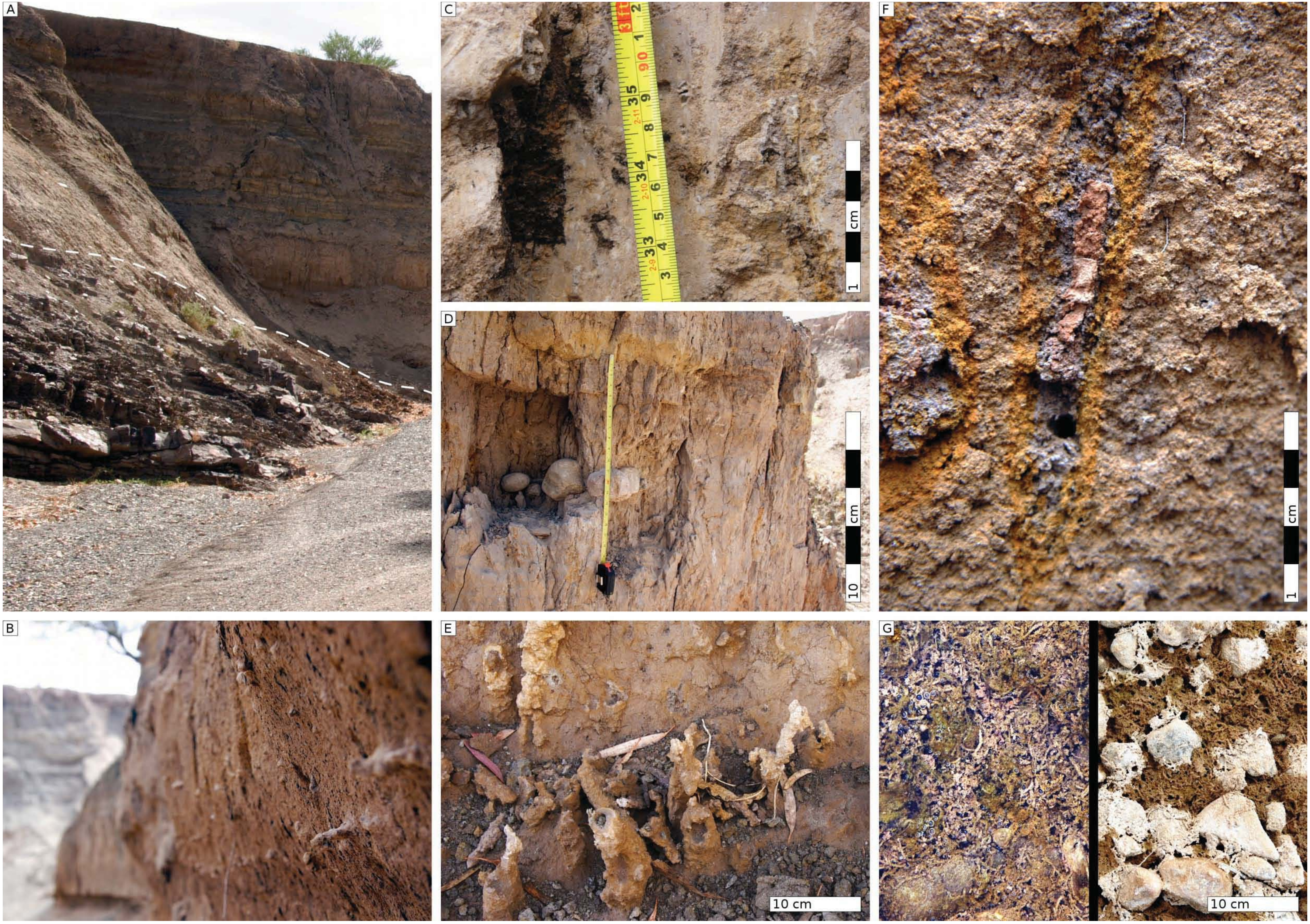
A
B
C
1
cm
D
10
cm
E
10 cm
F
1
cm
G
10 cm

(see opposite page)

Photo Plate 3) *Lithostratigraphic details:* ***A)*** *detail of the central aggradational sequence, indicating the boundaries between the lower lithostratigraphic units (I-II) above the palaeosol and the laminated units (II-III) above the 470-479 red band. The lithofacies that comprise the laminations are deposited as a cyclic sequence of yellow bands, veneers of organic detritus and partially discontinuous sheets of in situ tufa precipitates;* ***B)*** *insular remnant of the red surface drape, here sloping down the bank of Etina Creek, dissected by steep gullies of possibly post-European age;* ***C)*** *gravel exposure close to the present confluence of the Brachina and Etina Creeks with a general direction towards BRA-SD. Reversed directions of inclinations ("herringbone pattern") suggest flow directions in and out;* ***D)*** *wet-sieved residua (>200 µm) from the palaeosol (506-516) consisting of well-rounded sand-sized quartz particles;* ***E)*** *wet-sieved residua (>200 µm) from the basal unit (650-660) comprising two intact undissolved carbonate shells of the snails Charopidae sp. (left) and Austropyrgus sp. (Hydrobiidae) (right), today associated with damp vegetation and springs in the catchments of the Flinders Ranges (Glasby et al., 2007);* ***F)*** *wet-sieved residua (>200 µm) from the 470-479 red band comprising abundant detrital iron oxide-cemented pseudomorphs;* ***G)*** *wet-sieved residua (>200 µm) from the 373-380 yellow band comprising in situ tubular tufa cementation.*


A
10
cm
B
1 m
C
1 m
D
1 mm
E
1 mm
F
1 mm
G
1 mm

Acknowledgements

We thank CRC LEME (Cooperative Research Centre for Landscape Environments and Mineral Exploration), the Australian Research Council (ARC Environmental Futures Network grant DP0559577) and the Australian Institute of Nuclear Science and Engineering (AINSE Grants 96/192R, 99/001 and 07/160) for generous financial are consistent with in dating the stratigraphic section. The International Association of Sedimentologists (1st IAS 2008 postgraduate grant scheme) and Intellection Pty Ltd. are thanked for covering the costs pioneering the application of QEMSCAN® to questions of Quaternary stratigraphy and climate change, the Flinders Ranges National Park authorities for research permits and friendly accommodation, Jayesh Pillarisetty, Frances Williams, Rosi Glasby and Jutta von dem Bussche, for assisting in the field. In particular, we are indebted to Amy Suto from the University of Adelaide for helping to prepare the carbon stable isotope samples and Stewart Fallon from the Australian National University Radiocarbon Dating Laboratory for his work on the labour-intensive radiocarbon samples based on organic veneers, Craig C. Strong from Griffith University for introduction and assistance in the Particle Sizing Laboratory, and Rob Fitzpatrick from the University of Adelaide for kindly providing instrument time on his Bartington Magnetic Susceptibility System.

References

Aitken, M.J., 1998. *An Introduction to Optical Dating*. University Press, Oxford.

Bartington Instruments, 2007. *MS2 Magnetic Susceptibility System*. Bartington Instruments Ltd, Oxford.

Baruch, Z., 1994. Responses to drought and flooding in tropical forage grasses. *Plant and Soil.* 164(1), 87-96.

Beckman Coulter, 2002. Multisizer 3 Operator's Manual PN8321681 Rev. B. Beckman Coulter, Inc, Fullerton, California.

Blong, R.J., Gillespie, R., 1978. Fluvially transported charcoal gives erroneous ^{14}C ages for recent deposits. *Nature*. 271, 739-741.

Bowman, S., 1990. *Interpreting the Past: Radiocarbon Dating*. University of California Press, Berkeley.

Butler, B.E., 1955. A system for the description of soil structure and consistence in the field. *Journal of the Australian Institute of Agricultural Science*. 1, 231-252.

Callen, R.A., 1984. The islands of Lake Frome. Geological Survey of South Australia. *Quarterly Geological Notes*. 88, 2-8.

Cock, B.J., Williams, M.A.J., Adamson, D.A., 1999. Pleistocene Lake Brachina: a preliminary stratigraphy and chronology of lacustrine sediments from the central Flinders Ranges, South Australia. *Australian Journal of Earth Sciences*. 46, 61-69.

Crouvi, O., Amit, R., Enzel, Y., Porat, N., Sandler, A., 2008. Sand dunes as a major proximal dust source for late Pleistocene loess in the Negev Desert, Israel. *Quaternary Research*. 70 (2), 275-282.

Duller, G.A.T., 2004. Luminescence dating of Quaternary sediments: recent advances. *Journal of Quaternary Science*. 19 (2), 183-192.

Ehleringer, J.R., Cerling, T.E., Helliker, B.R., 1997. C4 photosynthesis, atmospheric CO_2, and climate. *Oecologia*. 112 (3), 285-299.

Eitel, B., Blümel, W.D., Hüser, K., Mauz, B., 2001. Dust and loessic alluvial deposits in Northwestern Namibia (Damaraland, Kaokoveld): sedimentology and palaeoclimatic evidence based on luminescence data. *Quaternary International*. 76, 57-65.

Farquhar, G.D., Ehleringer, J.R., Hubick, K.T., 1989. Carbon isotope discrimination and photosynthesis. *Annual Review of Plant Physiology and Plant Molecular Biology*. 40, 503-537.

Folk, R.L., 1971. Longitudinal dunes of the northwestern edge of the Simpson Desert, Northern Territory, Australia. 1. Geomorphology and grain size relationships. *Sedimentology*. 16, 5-54.

Folk, R.L., Ward, W.C., 1957. Brazos River bar: a study in the significance of grain size parameters. *Journal of Sedimentary Petrology*. 27 (1), 3-26.

Fifield, K., Chappell, J., Fallon, S.J., 2007. The new radiocarbon AMS system at the ANU. *Quaternary International*. 167-168, 116.

Fine, P., Verosub, K.L., Singer, M.J., 1995. Pedogenic and lithogenic contributions to the magnetic susceptibility record of the Chinese loess/palaeosol sequence. *Geophysical Journal International*. 122 (1), 97-107.

Fink, D., Hotchkis, M., Hua, Q., Jacobsen, G., Smith, A.M., Zoppi, U., Child, D., Mifsud, C., van der Gaast, H., Williams, A., Williams, M., 2004. The ANTARES AMS facility at ANSTO. *Nuclear Instruments and Methods in Physics Research Section B*. 223-224, 109-115.

Finlay, J.C., Kendall, C., 2007. Stable isotope tracing of temporal and spatial variability in organic matter sources to freshwater ecosystems. In: Michener, R., Lajtha, K. (Eds.), *Stable isotopes in Ecology and Environmental Science, 2nd Edition*. Wiley-Blackwell, pp. 283-333.

Fitzsimmons, K.E., Bowler, J.M., Rhodes, E.J., Magee, J.M., 2007. Relationships between desert dunes during the late Quaternary in the Lake Frome region, Strzelecki Desert, Australia. *Journal of Quaternary Science*. 22 (5), 549-558.

Galloway, R.W., 1965. Late Quaternary climates in Australia. *Journal of Geology*. 73 (4), 603–618.

Gasse, F., Chalié, F., Vincens, A., Williams, M.A.J., Williamson, D., 2008. Climatic patterns in equatorial and southern Africa from 30,000 to 10,000 years ago reconstructed from terrestrial and near-shore proxy data. *Quaternary Science Reviews*. 27, 2316-2340.

Gentilli, J., 1986. Climate. In: Jeans, D.N. (Ed.), *Australia - A Geography. The Natural Environment*. Sydney University Press, Sydney, pp. 14–48.

Glasby, P., Williams, M.A.J., McKirdy, D., Symonds, R., Chivas, A.R., 2007. Late Pleistocene environments in the Flinders Ranges, Australia: preliminary evidence from microfossils and stable isotopes. *Quaternary Australasia*. 24 (2), 19-28.

Gottlieb, P., Wilkie, G., Sutherland, D., Ho-Tun, E., Suthers, S., Perera, K., Jenkins, B., Spencer, S., Butcher, A., Rayner, J., 2000. Using quantitative electron microscopy for process mineralogy applications. *JOM Journal of the Minerals, Metals and Materials Society*. 52 (4), 24-25.

Haberlah, D., 2007: Depositional models of late Pleistocene fine-grained valley-fill deposits in the Flinders Ranges, SA. In: Fitzpatrick, R.W., Shand, P. (Eds) 2007, *Regolith 2006—Consolidation and dispersion of ideas*. Cooperative Research Centre for Landscape Environments and Mineral Exploration, Perth, pp. 122-126

Haberlah, D., McTainsh, G.H., *submitted*. Quantifying aggregation in sediments.

Haberlah, D., Williams, M.A.J., Hill, S.M., Halverson, G., Glasby, P., 2007. A terminal Last Glacial Maximum (LGM) loess-derived palaeoflood record from South Australia? *Quaternary International*. 167-168 Supplement, 150.

Haberlah, D., Glasby, P., Williams, M.A.J., Hill, S.M., Williams, F., Rhodes, E.J., Gostin, V., O'Flanery, A., Jacobsen, G.E., *in press*. 'Of droughts and flooding rains'*: an alluvial loess record from central South Australia spanning the last glacial cycle. In: Bishop, P., Pillans, B. (Eds.), *Australian Landscapes*. Geological Society Special Publications, London.

Hartley, A.J., Mather, A.E., Jolley, E., Turner, P., 2005. Climatic controls on alluvial-fan activity, Coastal Cordillera, northern Chile. *Geological Society London Special Publications*. 251 (1), 95-116.

Harvey, A.M., Wells, S.G., 1994. Late Pleistocene and Holocene changes in hillslope sediment supply to alluvial fan systems: Zzyzx, CA. In: Millington, A.C., Pye, K. (Eds.), *Environmental Change in Drylands*. Wiley, New York, pp. 66–84.

Heckathorn, S.A., McNaughton, S.J., Coleman, J.S., 1999. C_4 plants and herbivory. In: Sage, R.F., Monson, K. (Eds.), *C_4 Plant Biology*. Academic Press Ltd, London, pp. 285–312.

Heine, K., Heine, J.T., 2002. A paleohydrologic reinterpretation of the Homeb Silts, Kuiseb River, central Namib Desert (Namibia) and paleoclimatic implications. *Catena*. 48, 107-130.

Heine, K., Völkel, J. 2009. Desert flash flood series – Slackwater deposits and floodouts in Namibia: their significance for palaeoclimatic reconstructions. *Zentralblatt für Geologie und Paläontologie, Teil 1.* 3-4, 287-308.

Heller, F., Liu, T., 1984. Magnetism of Chinese loess deposits. *Geophysical Journal International*. 77 (1), 125-141.

Hessel, R., 2006. Consequences of hyperconcentrated flow for process-based soil erosion modelling on the Chinese Loess Plateau. *Earth Surface Processes and Landforms*. 31 (9), 1100-1114.

Hua, Q., Jacobsen, G.E., Zoppi, U., Lawson, E.M., Williams, A.A., Smith, A.M., McGann, M.J., 2001. Progress in radiocarbon target preparation at the ANTARES AMS centre. *Radiocarbon*. 43 (2A), 275–282.

Huang, C.C., Pang, J., Zha, X., Su, H., Jia, Y., Zhu, Y., 2007. Impact of monsoonal climatic change on Holocene overbank flooding along Sushui River, middle reach of the Yellow River, China. *Quaternary Science Reviews*. 26 (17-18), 2247-2264.

Hugenholtz, C.H., Wolfe, S.A., 2005. Biogeomorphic model of dunefield activation and stabilization on the northern Great Plains. *Geomorphology*. 70, 53–70.

Inman, D.L., 1952. Measures of describing the size distribution of sediments. *Journal of Sedimentary Petrology*. 22 (3), 125-145.

Johnson, B.J., Miller, G.H., Magee, J.W., Gagan, M.K., Fogel, M.L., Quay, P.D., 2005. Carbon isotope evidence for an abrupt reduction in grasses coincident with European settlement of Lake Eyre, South Australia. *The Holocene*. 15 (6), 888-896.

Kandler, K., Schütz, L., Deutscher, C., Ebert, M., Hofmann, H., Jäckel, S., Jaenicke, R., Knippertz, P., Lieke, K., Massling, A., Petzold, A., Schladitz, A., Weinzierl, B., Wiedensohler, A., Zorn, S., Weinbruch, S., 2009. Size distribution, mass concentration, chemical and mineralogical composition and derived optical parameters of the boundary layer aerosol at Tinfou, Morocco, during SAMUM 2006. *Tellus*. 61B, 32-50.

Kochel, R.C., Baker, V.R., 1988. Paleoflood analysis using slackwater deposits. In: Baker, V. R., Kochel, R.C. (Eds.), *Flood Geomorphology*. Wiley, New York, pp. 357-376.

Lambeck, K., Yokoyama, Y., Purcell, T., 2002. Into and out of the Last Glacial Maximum: sea-level change during Oxygen Isotope Stages 3 and 2. *Quaternary Science Reviews*. 21, 343–360.

Lancaster, N., 1994. Controls on aeolian activity: some new perspectives from the Kelso Dunes, Mojave Desert, California. *Journal of Arid Environments*. 27, 113-125.

Lancaster, N., 2002. How dry was dry? Late Pleistocene palaeoclimates in the Namib Desert. *Quaternary Science Reviews*. 21 (7), 769-782.

Leng, M.J., Lamb, A.L., Heaton, T.H.E., Marshall, J.D., Wolfe, B.B., Jones, M.D., Holmes, J.A., Arrowsmith, C., 2005. Isotopes in lake sediments. In: Leng, M.J. (Ed.), *Isotopes in Palaeoenvironmental Research*. Springer, Dordrecht, The Netherlands, pp. 148-176.

Leys, J., McTainsh, G., Koen, T., Mooney, B., Strong, C., 2005. Testing a statistical curve-fitting procedure for quantifying sediment populations within multi-modal particle-size distributions. *Earth Surface Processes and Landforms*. 30, 579-590.

Liu, W., Huang, Y., An, Z., Clemens, S.C., Li, L., Prell, W.L., Ning, Y., 2005. Summer monsoon intensity controls C_4/C_3 plant abundance during the last 35 ka in the Chinese Loess Plateau: Carbon isotope evidence from bulk organic matter and individual leaf waxes. *Palaeogeography, Palaeoclimatology, Palaeoecology*. 220 (3-4), 243-254.

Luly, J.G., Jacobson, G., 2000. Two new AMS dates from Lake Frome, arid South Australia. *Quaternary Australasia*. 18, 29-33.

Macdonald, P.D.M., Du, J., 2004. Mixdist: Mixture Distribution Models. R package version 0.5-1. Available at: http://www.math.mcmaster.ca/peter/mix/mix.html [Accessed 30/05/2008].

Maher, B.A., 1998. Magnetic properties of modern soils and Quaternary loessic paleosols: paleoclimatic implications. *Palaeogeography, Palaeoclimatology, Palaeoecology*. 137 (1-2), 25-54.

van Maren, D.S., Winterwerp, J.C., Wu, B.S., Zhou, J.J., 2009. Modelling hyperconcentrated flow in the Yellow River. *Earth Surface Processes and Landforms*. 34 (4), 596-612.

Marshall, J.D., Brooks, J.R., Lajtha, K., 2007. Sources of variation in the stable isotope composition of plants. In: Michener, R., Lajtha, K. (Eds.), *Stable isotopes in Ecology and Environmental Science*. Wiley-Blackwell, Malden, MA, pp. 22-60.

McCarthy, D., Rogers, T., Casperson, K. (Eds.), 2006. *Floods in South Australia, 1836-2005*. Bureau of Meterology South Australian Regional Office, Kent Town, South Australia.

McIntyre, D.S., 1976. Subplasticity in Australian soils. 1 description, occurrence, and some properties. *Australian Journal of Soil Research*. 14, 227-236.

Mix, A.C., Bard, E., Schneider, R., 2001. Environmental processes of the ice age: land, oceans, glaciers (EPILOG). *Quaternary Science Reviews*. 20, 627-657.

Newnham, R.M., Lowe, D.J., Giles, T., Alloway, B.V., 2007a. Vegetation and climate of Auckland, New Zealand, since ca. 32 000 cal. yr ago: are consistent with for an extended LGM. *Journal of Quaternary Science*. 22 (5), 517-534.

Newnham, R.M., Vandergoes, M.J., Hendy, C.H., Lowe, D.J., Preusser, F., 2007b. A terrestrial palynological record for the last two glacial cycles from southwestern New Zealand. *Quaternary Science Reviews*. 26, 517–535.

Olley, J.M., Caitcheon, G., Murray, A.S., 1998. The distribution of apparent dose as determined by optically stimulated luminescence in small aliquots of fluvial quartz: implications for dating young sediments. *Quaternary Geochronology*. 17, 1033-1040.

Olsson, I., 1986. Radiometric methods. In: Berglund, B.E., Ralska-Jasiewiczowa, M. (Eds.), *Handbook of Holocene Palaeoecology and Palaeohydrology*. Wiley, Chichester, pp. 273-312.

Pedley, M., 2009. Tufas and travertines of the Mediterranean region: a testing ground for freshwater carbonate concepts and developments. *Sedimentology*. 56 (1), 221-246.

Petherick, L.M., McGowan, H.A., Moss, P., 2008. Climate variability during the Last Glacial Maximum in eastern Australia: evidence of two stadials? *Journal of Quaternary Science*. 23, 787-802.

Petherick, L.M., McGowan, H.A., Kamber, B.S., 2009. Reconstructing transport pathways for late Quaternary dust from eastern Australia using the composition of trace elements of long traveled dusts. *Geomorphology*. 105, 67-79.

Quigley, M.C., Sandiford, M., Cupper, M.L., 2007. Distinguishing tectonic from climatic controls on range-front sedimentation. *Basin Research*. 19 (4), 491-505.

Preiss, W.V. (Ed.), 1987. *The Adelaide Geosyncline: Late Proterozoic stratigraphy, sedimentation, palaeontology and tectonics*. Dept. of Mines and Energy, Geol. of Survey South Australia, Adelaide.

R Development Core Team, 2008. R: A Language and Environment for Statistical Computing. R Foundation for Statistical Computing. Vienna, Austria, Available at: http://www.r-project.org/ [Accessed May 30, 2008].

Revel-Rolland, M., De Deckker, P., Delmonte, B., Hesse, P.P., Magee, J.W., Basile-Doelsch, I., Grousset, F., Bosch, D., 2006. Eastern Australia: a possible source of dust in East Antarctica interglacial ice. *Earth and Planetary Science Letters*. 249 (1-2), 1-13.

Rögner, K., Knabe, K., Roscher, B., Smykatz-Kloss, W., Zöller, L., 2004. Alluvial loess in the Central Sinai: occurrence, origin, and palaeoclimatological consideration. *Paleoecology of Quaternary Drylands. Lecture Notes in Earth Sciences*. 102, 79-99.

Rust, B.R., 1972., Pebble orientation in fluvial sediments. *Journal of Sedimentary Petrology*. 42 (2), 384-388.

Sage, R.F., Coleman, J.R., 2001. Effects of low atmospheric CO_2 on plants: more than a thing of the past. *Trends in Plant Science*. 6 (1), 18-24.

Schieber, J., Southard, J., Thaisen, K., 2007. Accretion of mudstone beds from migrating floccule ripples. *Science*. 318, 1760-1763.

Schmid, R.M., 1990. Absolute dating of sedimentation on Lake Torrens with spring deposits, South Australia. *Hydrobiologia*. 197, 305-308.

Shulmeister, J., Goodwin, I., Renwick, J., Harle, K., Armand, L., McGlone, M.S., Cook, E., Dodson, J., Hesse, P.P., Mayewski, P., Curran, M., 2004. The Southern Hemisphere westerlies in the Australasian sector over the last glacial cycle: a synthesis. *Quaternary International*, 118-119, 23-53.

Singh, G., Luly, J.G., 1991. Changes in vegetation and seasonal climate since the last full glacial at Lake Frome, South Australia. *Palaeogeography, Palaeoclimatology, Palaeoecology*. 84, 75-86.

Srivastava, P., Brook, G.A., Marais, E., 2005. Depositional environment and luminescence chronology of the Hoarusib River Clay Castles sediments, northern Namib Desert, Namibia. *Catena*. 59 (2), 187-204.

Srivastava, P., Brook, G.A., Marais, E., Morthekai, P., Singhvi, A.K., 2006. Depositional environment and OSL chronology of the Homeb silt deposits, Kuiseb River, Namibia. *Quaternary Research*. 65 (3), 478-491.

Suggate, R.P., Almond, P.C., 2005. The Last Glacial Maximum (LGM) in western South Island, New Zealand: implications for the global LGM and MIS 2. *Quaternary Science Reviews*. 24, 1923–1940.

Sun, J. 2002. Provenance of loess material and formation of loess deposits on the Chinese Loess Plateau. *Earth and Planetary Science Letters*. 203, 845-859.

Sun, D., Bloemendal, J., Rea, D.K., Vandenberghe, J., Jiang, F., An, Z., Su, R., 2002. Grain-size distribution function of polymodal sediments in hydraulic and aeolian environments, and numerical partitioning of the sedimentary components. *Sedimentary Geology*. 152, 263-277.

Sutherland, D., 2007. Estimation of mineral grain size using automated mineralogy. *Minerals Engineering*. 20 (5), 452-460.

Tipple, B.J., Pagani, M., 2007. The early origins of terrestrial C_4 photosynthesis. *Annual Review of Earth and Planetary Sciences*. 35, 435-461.

Weninger, B., Jöris, O., 2008. A ^{14}C age calibration curve for the last 60 ka: the Greenland-Hulu U/Th timescale and its impact on understanding the Middle to Upper Paleolithic transition in Western Eurasia. *Journal of Human Evolution*. 55 (5), 772-781.

Weninger, B., Jöris, O., Danzeglocke, U., 2008. CalPal-2007. Cologne Radiocarbon Calibration & Palaeoclimate Research Package. Available at: http://www.calpal.de [Accessed 28/04/2009].

Williams, M.A.J., Nitschke, N., 2005. Influence of wind-blown dust on landscape evolution in the Flinders Ranges, South Australia. *South Australian Geographical Journal*. 104, 25-36.

Williams, M.A.J., Prescott, J.R., Chappell, J., Adamson, D., Cock, B., Walker, K., Gell, P., 2001. The enigma of a late Pleistocene wetland in the Flinders Ranges, South Australia. *Quaternary International*. 83-85, 129-144.

Williams, M.A.J., Nitschke, N., Chor, C., 2006. Complex geomorphic response to late Pleistocene climatic changes in the arid Flinders Ranges of South Australia. *Géomorphologie: relief, processus, environnement*, 4, 249-258.

Williams, M., Cook, E., van der Kaars, S., Barrows, T., Shulmeister, J., Kershaw, P., 2009. Glacial and deglacial climatic patterns in Australia and surrounding regions from 35 000 to 10 000 years ago reconstructed from terrestrial and near-shore proxy data. *Quaternary Science Reviews*. doi:10.1016/j.quascirev.2009.04.020

Zhou, L.P., Oldfield, F., Wintle, A.G., Robinson, S.G., Wang, J.T., 1990. Partly pedogenic origin of magnetic variations in Chinese loess. *Nature*. 346, 737-739.

Zielhofer, C., Faust, D., 2008. Mid- and Late Holocene fluvial chronology of Tunisia. *Quaternary Science Reviews*. 27 (5-6), 580-588.